

Nonlinear quadrupole topological insulators

Ruijiang Li^{a,*}, Wencai Wang^a, Yongtao Jia^a, Ying Liu^a, Pengfei Li^{b,c}, Boris A. Malomed^{d,e}

^a*National Key Laboratory of Radar Detection and Sensing, School of Electronic Engineering, Xidian University, Xi'an, 710071, China*

^b*Department of Physics, Taiyuan Normal University, Jinzhong, 030619, China*

^c*Institute of Computational and Applied Physics, Taiyuan Normal University, Jinzhong, 030619, Shanxi, China*

^d*Department of Physical Electronics, School of Electrical Engineering, Faculty of Engineering, Tel Aviv University, Tel Aviv, 69978, Israel*

^e*Instituto de Alta Investigación, Universidad de Tarapacá, Casilla 7D, Arica, Chile*

Abstract

Higher-order topological insulators (HOTIs) represent a family of topological phases that go beyond the conventional bulk-boundary correspondence. d -dimensional n -th order HOTIs maintain $(d - n)$ -dimensional gapless boundary states (in particular, zero-dimensional corner states in the case of $d = n = 2$). HOTIs of the Wannier type can be extended into the nonlinear regime. Another prominent class of HOTIs, in the form of multipole insulators, was investigated only in the linear regime, due to the challenge of simultaneously achieving both negative hopping and strong nonlinearity. Here we propose the concept of nonlinear quadrupole topological insulators (NLQTIs) and report their *experimental realization* in an electric circuit lattice. Quench-initiated dynamics gives rise to nonlinear topological corner states and topologically trivial corner solitons, in weakly and strongly nonlinear regimes, respectively. Furthermore, we reveal the formation of two distinct types of bulk solitons, one existing in the middle finite gap under the action of weak nonlinearity, and another one found in the semi-infinite gap under strong nonlinearity. This work realizes another member of the nonlinear HOTI family, suggesting directions for exploring novel solitons across a broad range of topological insulators.

Keywords: Quadrupole topological insulators, Nonlinear higher-order topological insulators, Nonlinear corner states, Bulk solitons, Topological circuits

1. Introduction

Standard topological insulators (TIs) maintain topological edge states with dimension lower by 1 than that of the bulk [1, 2]. Extending the notion of the electric polarization to higher-order multipole moments, TIs with a multipole structure have been proposed [3, 4]. They represent higher-order topological phases extending the conventional bulk-boundary correspondence. In particular, a two-dimensional (2D) quadrupole topological insulator (QTI) features the hallmark of topologically protected zero-dimensional corner states. This possibility addresses the long-standing issue of whether higher multipole moments can take quantized values and thus maintain topological phases, a problem that remained unresolved for a long time. Multipole TIs have been realized in various physical systems, including mechanical [5], photonic [6, 7], electric-circuit [8, 9, 10, 11], and acoustic [12, 13, 14, 15] lattices, a crucial step being the implementation of positive and negative hoppings in them, where the positive hopping corresponds to the coupling of adjacent lattice sites with no phase shift, while the negative hopping carries a phase shift of π (the sign inversion) [6, 13, 14]. These hoppings can be implemented in staggered optical and matter-wave settings [16, 17] and in electric-circuit lattices with an appropriate combination of capacitors

and inductors [8, 9, 10, 11]. On the other hand, to eliminate the requirement of the negative hopping, another class of HOTIs, based on “quantized” Wannier centers (ones with discrete location of their centers), was proposed [18, 19] and experimentally demonstrated in a variety of physical setups [20, 21, 22, 23, 24, 25, 26, 27, 28, 29, 30, 31].

There is growing interest in exploring the interplay between topological states and intrinsic nonlinearity in standard (first-order) TIs [32, 33, 34, 35, 36] and higher-order TIs (HOTIs) [37, 38, 39, 40]. Nonlinearity not only extends topological states from the linear limit [41, 42, 43, 44, 45, 46, 47, 48, 49, 50, 51, 52, 53, 54, 55], but also gives rise to bulk solitons that do not exist in the linear regime [55, 56, 57, 58, 59, 60, 61, 62, 63, 64]. Building on theoretical studies [65, 66, 67, 68, 69, 70, 71], nonlinear Wannier-type HOTIs have been experimentally demonstrated, featuring topological phase transitions [72], higher-order topological bound states in the continuum [73], and formation of nonlinear topological corner states, along with topologically trivial corner solitons [74]. In contrast, multipole TIs, while being the earliest proposed and most representative type of HOTIs, have been addressed only in the framework of the linear regime, primarily due to the challenges of realizing the negative hopping and strong nonlinearity simultaneously. QTIs with externally controlled hoppings also remain essentially linear objects, as they lack amplitude-dependent self-interaction [75].

The objective of the present work is to introduce the con-

*Corresponding author.

Email address: ruijiangli@xidian.edu.cn (Ruijiang Li)

cept of nonlinear QTIs (NLQTIs) and *experimentally demonstrate* their realization in an electric-circuit lattice. Similar to the nonlinear Wannier-type HOTIs realized in evanescently-coupled optical-waveguide lattices [74], we initiate dynamical regimes by the application of quench and observe the excitation of NLQTIs in the form of weakly nonlinear topological corner states and strongly nonlinear topologically trivial corner solitons. Additionally, we discover the formation of two distinct types of bulk solitons, *viz.*, weakly and strongly nonlinear ones, which populate the middle finite bandgap and semi-infinite gap, respectively. These solitons have not been predicted or observed before in nonlinear HOTIs (including nonlinear Wannier-type ones). Thus, the present work extends multipole TIs, in the form of NLQTIs, into the nonlinear regime. Since only two types of HOTIs have been discovered so far, our NLQTI may be considered as the another constituent of the nonlinear HOTI family. Further, our results overcome the previous limitation which implied that bulk solitons were only found in the standard (first-order) TIs [57, 58, 60]. This framework can be further extended to include nonlinear octupole and hexadecapole TIs, hence our findings suggest new directions for exploring solitons in a broad range of TIs.

2. Results

2.1. The tight-binding model and circuit lattice

The tight-binding lattice supporting NLQTIs is presented in Fig. 1(a). Each unit cell consists of four lattice sites, with the (m, n) -th unit cell indicated by the purple square. The intracell and intercell hopping strengths are denoted as γ and λ , respectively, with solid and dashed lines designating positive and negative hoppings. Unlike the linear QTI [3], in Fig. 1(a) it is shown that the onsite energies in our NLQTI, $\delta_{m,n}^{(j)}$, $j = 1, 2, 3, 4$, depend on the wave functions $\psi_{m,n}^{(j)}$ at the respective sites. In photonic and bosonic-gas systems, these dependences are typically represented by quadratic forms [76, 77, 78, 79] (see further details in Appendix A for the model of the interacting bosonic gas). Here we realize this tight-binding model, using the electric-circuit lattice shown in Fig. 1(b). The circuit elements (C_1, L_1) and (C_2, L_2) determine the intracell and intercell hoppings, respectively. To implement the amplitude-dependent onsite energies, we employ two types of grounded nonlinear oscillators. Circuit nodes 1 and 4 are connected to inductors L_g , L_1 , L_2 and common-cathode diodes C_v , while nodes 2 and 3 are connected to capacitors C_1 and C_2 , along with inductors L_g and common-cathode diodes C_v . The common-cathode diodes function as voltage-dependent capacitors, with capacitance

$$C(v) = \frac{C_L}{(1 + |v/v_0|)^M}, \quad (1)$$

where v is the voltage amplitude, with constants chosen here as $C_L = 8.6$ nF, $v_0 = 1.7$, and $M = 0.3$ (see details in Appendix B.1).

The voltages at the circuit nodes in the (m, n) -th unit cell, denoted as $\psi_{m,n}^{(j)}$ with $j = 1, 2, 3, 4$, satisfy the following equation

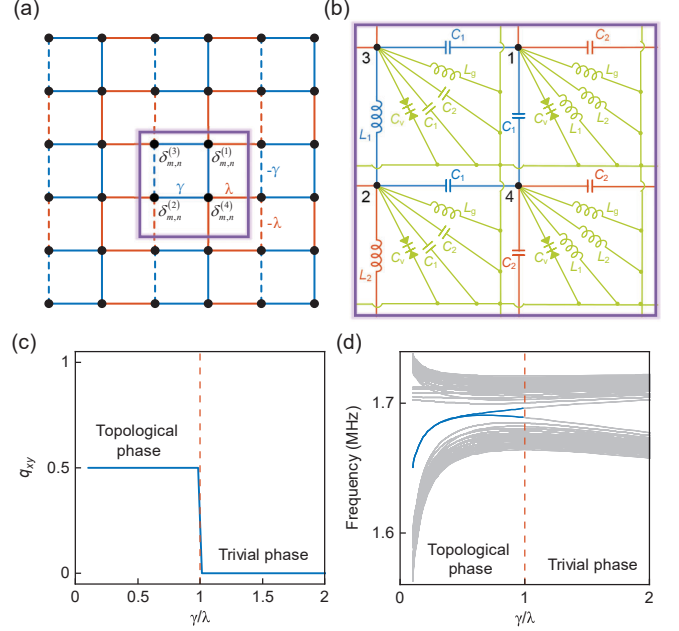


Figure 1: **Schematic representation of the nonlinear quadrupole topological insulator (NLQTI) and its topological properties in the linear limit.** (a) The tight-binding lattice model of the NLQTI, where γ and λ represent the intracell and intercell hopping strengths, respectively. Solid and dashed lines designate positive and negative hoppings, respectively. Parameters $\delta_{m,n}^{(1,2,3,4)}$ denote the amplitude-dependent onsite energies in the (m, n) -th unit cell. (b) The unit cell of the electric-circuit lattice realizing the NLQTI. Blue and red circuit elements realize the intracell and intercell hoppings, respectively, while yellow-green grounded circuit elements determine the onsite energies. (c) The dependence of the quadrupole moment q_{xy} on the dimerization ratio γ/λ . (d) The frequency spectrum of the lattice with open boundary conditions in the x and y directions, plotted as a function of γ/λ . The blue curve indicates the corner states, while the gray curves denote the bulk and edge ones. The red lines in (c) and (d) mark the phase-transition boundary.

(for the detailed derivation, see Appendix B.2):

$$i \frac{d\Psi}{dt} = \mathbf{H}\Psi, \quad (2)$$

where $\Psi = [\psi_{m,n}^{(1)}, \psi_{m,n}^{(2)}, \psi_{m,n}^{(3)}, \psi_{m,n}^{(4)}]^T$, with T denoting the transpose of the vector. The Hamiltonian \mathbf{H} is defined as

$$\mathbf{H} = \begin{pmatrix} \delta_{m,n}^{(1)} & 0 & \mathbf{C}_{1,0} & \mathbf{C}_{0,1} \\ 0 & \delta_{m,n}^{(2)} & -\mathbf{C}_{0,-1} & \mathbf{C}_{-1,0} \\ \mathbf{C}_{-1,0} & -\mathbf{C}_{0,1} & \delta_{m,n}^{(3)} & 0 \\ \mathbf{C}_{0,-1} & \mathbf{C}_{1,0} & 0 & \delta_{m,n}^{(4)} \end{pmatrix}, \quad (3)$$

where $\mathbf{C}_{k,l} = \gamma + \lambda \mathbf{T}_{k,l}$ and the discrete translational operator is defined as $\mathbf{T}_{k,l} \psi_{m,n}^{(j)} = \psi_{m+k, n+l}^{(j)}$. In Eq. (3), the above-mentioned amplitude-dependent onsite energies are $\delta_{m,n}^{(j)} = \delta_0 + g(\psi_{m,n}^{(j)})$, where $\delta_0 = [1 - \frac{C_1+C_2}{C_L} + \frac{L_g}{2} (\frac{1}{L_1} + \frac{1}{L_2})] \omega_0$ and $g(\psi_{m,n}^{(j)}) = -\frac{C_v(\psi_{m,n}^{(j)}) - C_L}{2C_L} \omega_0$, with $\omega_0 = 1/\sqrt{L_g C_L}$ and $C_v(\psi_{m,n}^{(j)})$ defined as per Eq. (1), with v substituted by the respective $\psi_{m,n}^{(j)}$. The intracell and intercell hopping strengths are $\gamma = \frac{C_1}{2C_L} \omega_0 = \frac{L_g}{2L_1} \omega_0$ and $\lambda = \frac{C_2}{2C_L} \omega_0 = \frac{L_g}{2L_2} \omega_0$, respectively. We set $L_g = 1$ μ H (recall H is the inductance unit, Henry) and adjust the values of L_1 and L_2 accordingly, while determining the values of the other

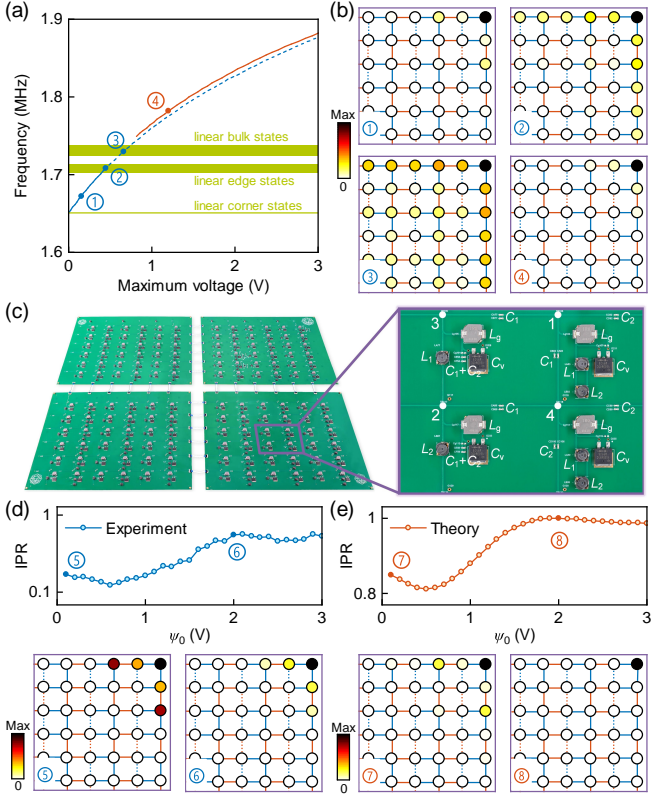


Figure 2: **Nonlinear topological corner states and topologically trivial corner solitons in the NLQTI.** (a) The dependence of the eigenfrequency on the maximum voltage in the lattice. The solid and dashed blue curves represent localized and delocalized nonlinear corner states, respectively, while the red curve pertains to the corner solitons. The frequencies corresponding to the linear corner, edge, and bulk states are indicated by the green regions. (b) Absolute values of the voltage distributions for the states labeled in (a), normalized to their respective maximum values. (c) The side view of the fabricated PCB, with the inset exhibiting the unit cell of the circuit lattice. The circuit elements are labeled in the inset. (d,e) Experimental and theoretical IPRs of the voltage distributions (see Eq. (4)) at $t = 9 \mu\text{s}$ for different initial voltages. Plots marked as ⑤ through ⑧ display the voltage distributions for the respective values of ψ_0 in panels (d) and (e).

circuit elements. In the linear limit, with $g = 0$, this circuit configuration satisfies two anti-commuting reflection symmetries, m_x and m_y , which quantize the quadrupole moment q_{xy} to either 0 or $\frac{1}{2}$ (for a detailed discussion, see Appendix C). Specifically, the system exhibits a topological quadrupole phase with $q_{xy} = \frac{1}{2}$ when $\gamma < \lambda$, and it is topologically trivial when $\gamma > \lambda$, as illustrated in Fig. 1(c). The corner states emerge due to the presence of the nontrivial bulk quadrupole moment, as highlighted by the blue curves in Fig. 1(d), which displays the frequency spectrum for a lattice with open boundary conditions in the x and y directions. The gray curves in Fig. 1(d) represent the bulk and edge states.

2.2. Nonlinear corner states and corner solitons: the theory and experiment

We set $L_1 = 150 \mu\text{H}$ and $L_2 = 15 \mu\text{H}$, defining $\Psi = \Phi e^{-i2\pi ft}$. The eigenfrequencies f and eigenstates Φ of the nonlinear quadrupole circuit, governed by Eqs. (2)-(3), were calculated

using Newton's algorithm (see Appendix D.1). Since the four linear corner states are equivalent to one another, in terms of both eigenfrequencies and eigenstates (see Fig. C.7), we focus on the nonlinear corner states and corner solitons localized at the upper-right corner of the lattice, as a relevant example.

Figure 2(a) displays the relationship between the eigenfrequency and maximum voltage. For comparison, the frequencies corresponding to the linear corner, edge, and bulk states are indicated by the green regions. The nonlinear corner states (plotted by the blue curve) bifurcate from the linear topological corner mode and remain well localized (see state ① in Fig. 2(b)). A similar phenomenon is observed in arrays of evanescently coupled waveguides with all-positive hoppings [74]. As the corner states are sublattice-polarized ones [80], the onsite energies can be approximated as $\delta_{m,n}^{(1)} = \delta_0 + g(\phi_{2,2}^{(1)})$ and $\delta_{m,n}^{(2,3,4)} = \delta_0$, where $\phi_{2,2}^{(1)}$ is the component of Φ representing the voltage at site 1 of the $(2, 2)$ -th unit cell, i.e., at the upper-right lattice corner. The reflection symmetries m_x and m_y are broken, resulting in the fact that the Wannier-state centers no longer satisfy the relations inherent from linear QTIs—specifically, one now has $v_{x,y}^- \neq -v_{x,y}^+ \pmod{1}$. Although the Wannier-sector polarizations p_y^{\pm} and p_x^{\pm} are no longer quantized, the quadrupole moment q_{xy} remains strictly positive, unlike its nearly zero value for a trivial insulator (see Appendix D.2) [73, 74]. Thus, the nonvanishing quadrupole invariant indicates that the corner states are topologically nontrivial modes, persisting in the presences of the onsite nonlinearity.

As the maximum voltage increases and the frequency enters the band of linear edge states, the nonlinear corner states hybridize with the edge ones and become delocalized (see Fig. 2(a) and state ② in Fig. 2(b)). The further increase in the eigenfrequency of the nonlinear corner states leads to additional delocalization through the hybridization with bulk modes (see Fig. 2(a) and state ③ in Fig. 2(b)). When the frequency continues to increase and enters the semi-infinite gap, the nonlinear corner states remain delocalized. This behavior is consistent with the previous observations in waveguide arrays [74]. Considering the delocalized field distributions, the previous approximation for the onsite energy becomes invalid, and the periodicity of the lattice is broken. As a result, the original definition of the quadrupole moment q_{xy} is no longer applicable. Due to the competition between the onsite self-interaction and inter-site hoppings, localized states do not exist in this moderately nonlinear regime.

In the regime of strong nonlinearity, a new branch corresponding to corner solitons emerges, indicated by the red curve in Fig. 2(a). These solitons arise at a nonzero voltage because they become too weakly localized at low voltages (see Appendix D.1), therefore the numerical method is unable to capture poorly localized solutions for a finite lattice, similar to the results reported in Ref. [49]. As these corner solitons are generally strongly localized at the corner sites and lack the sublattice polarization (see state ④ in Fig. 2(b)), the previous approximation, $\delta^{(1)} = \delta_0 + g(\phi_{2,2}^{(1)})$ and $\delta^{(2,3,4)} = \delta_0$, is no longer valid. Instead, when the onsite energies dominate over the differences between the intracell and intercell hop-

ping strengths, the NLQTI may be approximated as a nonlinear lattice with equal intracell and intercell hopping strengths $\frac{\gamma+\lambda}{2}$ (see Appendix D.2). This lattice exhibits no dimerization and supports conventional self-trapped states residing at the lattice edges, commonly referred to as surface solitons, which are topologically trivial modes [76, 77, 78]. Here, as such states are located at the corner, which is the junction of two edges, we call this special type of the surface modes *corner solitons* [73, 74]. As the maximum voltage increases to a sufficiently high level, Eqs. (2)-(3) reduce to $i\frac{d\psi_{2,2}^{(1)}}{dt} = \delta_{2,2}^{(1)}(\psi_{2,2}^{(1)})\psi_{2,2}^{(1)}$, governing the dynamics of the nonlinear single lattice site.

As both the localized nonlinear corner states and topologically trivial corner solitons are dynamically stable (see Fig. D.10 and Appendix D.3), we have verified their existence experimentally, through quench dynamics (see details in Appendix F) [81]. Figure 2(c) shows the circuit lattice fabricated as a printed circuit board (PCB), which carries a 6×6 array of unit cells. The inset displays the unit cell of the circuit lattice, with circuit elements labeled in it. For the experiment, the initial state at $t = 0$ was prepared as $\psi_{m,n}^{(i)}(t = 0) = \psi_0 \delta_{m,2} \delta_{n,2} \delta_{i,1}$, with a nonzero voltage applied solely at the upper-right corner site. The voltage distribution at $t \geq 0$ was recorded during the temporal evolution, using an oscilloscope. Subsequently, the envelope of the temporal voltage signals corresponding to $\psi_{m,n}^{(i)}(t)$ was extracted.

In the weakly nonlinear regime, when ψ_0 is small, the initial state can be expanded into a set of the eigenstates of the respective linear model: $\Psi(t = 0) = \sum_n c_n \Phi_n$, where c_n are expansion coefficients. Thus we found $\Psi(t) = \sum_n c_n e^{-i2\pi f_n t} \Phi_n$, with f_n being the eigenfrequency of the n -th eigenstate [67]. As the initial state largely overlaps with the corner one, the expansion coefficient corresponding to the corner state is close to 1, resulting in a localized voltage distribution with sublattice polarization as a result of the temporal evolution. Conversely, when ψ_0 attains a medium value, corresponding to the moderately nonlinear regime, we expect a delocalized voltage distribution due to the absence of localized eigenstates. When ψ_0 becomes sufficiently large (in the strongly nonlinear regime), the initial state predominantly overlaps with the eigenstate of the corner soliton. Particularly, in the ultra-strongly nonlinear regime, the initial state perfectly matches the single-site corner soliton, leading to the sharply localized topologically trivial voltage distributions.

We define the inverse participation ratio (IPR) as

$$\text{IPR} = \frac{\sum_{m,n,i} |\psi_{m,n}^{(i)}|^4}{\left(\sum_{m,n,i} |\psi_{m,n}^{(i)}|^2\right)^2}, \quad (4)$$

which measures the localization degree of the field distribution, with a higher IPR indicating stronger localization. Theoretically, the IPR should be evaluated after a sufficiently long evolution time. However, due to inevitable circuit dissipations in experiments, we extract the voltage distributions at $t = 9 \mu\text{s}$, with the corresponding IPR results for the experimental voltage distributions shown in Fig. 2(d). The insets ⑤ and ⑥ present

the voltage distributions for two representative values of ψ_0 . The theoretical results, derived from the numerical solutions of Eqs. (2)-(3), are displayed in Fig. 2(e). For comparison, the measurement result and theoretical predication of voltage distribution in the moderately nonlinear regime are shown in Fig. F.16(a).

From the results, we observe that the voltage distributions are localized for both small and large initial voltages, while they appear comparatively delocalized at medium initial voltage values. This localization-delocalization-localization transition indicates that nonlinear corner states and corner solitons are excited in the weakly and strongly nonlinear regimes, respectively, whereas no localized states exist in the medium-nonlinearity regime (see Fig. H.18 for an illustration of the transition and Appendix H for a relevant discussion). Although the circuit dissipation causes deviations in the specific values of the experimental result, it primarily induces an overall reduction in the IPRs, which are measured experimentally, and does not alter the overall trend, which agrees well with the theoretical prediction. This implies that the selection of the time moment $t = 9 \mu\text{s}$ is appropriate for observing the localization-delocalization-localization transition and for validating the existence of nonlinear corner states and corner solitons. Our conclusion is further supported by the result obtained for longer evolution times, where the localization-delocalization-localization transition is again observed (see Fig. G.17 and Appendix G).

2.3. Bulk solitons

We then focus on the solitons residing in the bulk of the NLQTI. In the anti-continuum limit [82], we identify solution branches for the bulk solitons, beginning with the ultimate case of the lattice without intersite hopping, wherein only two states are expected to be observed experimentally (see Appendix E for a detailed discussion).

Figure 3(a) displays the frequency spectra for these two types of bulk solitons. The frequencies corresponding to the linear corner, edge, and bulk states are indicated by the green regions. Although the bulk solitons are expected to approach the bulk bands in the linear limit [55], the termination of the soliton branches is, once again, explained by the weak localization of the solitons at low voltages (see Appendix E.2) and the limitation of the numerical algorithm. In the middle finite bandgap between two bands of the linear edge states, a single type exists, represented by the solid blue curve in Fig. 3(a). This soliton features a triangular quasi-antisymmetric profile, characterized by the relation $\psi_{0,0}^{(1)} \approx -\psi_{1,0}^{(3)} = -\psi_{0,1}^{(4)}$ (see state ① in Fig. 3(b)). Once the frequency of this soliton enters the edge band, it becomes a delocalized state, as indicated by the dashed blue curve in Fig. 3(a) and state ② in Fig. 3(b). A further increase in frequency results in hybridization with bulk states, causing the bulk soliton to become more delocalized, as shown by state ③ in Fig. 3(b). Additionally, a new branch for another type of the bulk solitons emerges in the semi-infinite gap, as shown by the solid red curve in Fig. 3(a). These solitons also exhibit quasi-antisymmetric profiles and remain localized (see state ④ in Fig. 3(b)). They correspond to conventional lattice solitons

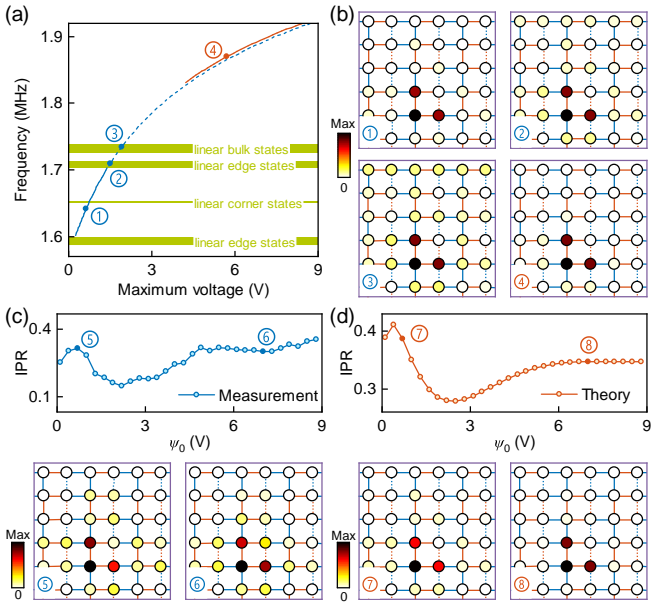


Figure 3: Bulk solitons in the NLQTI. (a) The eigenfrequency versus the maximum voltage in the lattice. The solid blue and red curves represent two distinct types of bulk solitons, both of which are localized states. The dashed blue curve indicates the delocalized states that arise from one type of the bulk soliton. For comparison, the frequencies corresponding to the linear corner, edge, and bulk states are indicated by the green regions. (b) Absolute values of the normalized voltage distributions for the quasi-antisymmetric triangular solitons labeled in (a). (c,d) Experimentally measured and theoretically predicted IPRs of the voltage distributions at $t = 8 \mu\text{s}$ for different initial voltages, with insets ⑤–⑧ showing the voltage distributions at representative values of ψ_0 .

residing in the bulk of the lattice, getting more localized as the nonlinearity strengthens [76, 77, 78]. Moreover, it is relevant to emphasize that both types of bulk solitons can still be found even if one swaps the intracell and intercell hopping strengths, thereby transforming the NLQTI into a lattice that is a topologically trivial QTI in the linear limit.

We explored the quench dynamics to experimentally verify the existence of the two theoretically predicted types of bulk solitons. Unlike the single-site excitation shown in Fig. 2, we prepared an initial state at $t = 0$ in a triangular quasi-antisymmetric form, with $\psi_{0,0}^{(1)} = -\psi_{1,0}^{(3)} = -\psi_{0,1}^{(4)} \equiv \psi_0$ and zero voltages at all other sites. The voltage distributions resulting from the temporal evolution were recorded, and voltage envelopes corresponding to $\psi_{m,n}^{(i)}(t)$ were extracted. At the selected moment $t = 8 \mu\text{s}$, the results shown in Figs. 3(c)-(d) reveal that the voltage distributions are localized for both small and large initial voltage values, while they appear comparatively delocalized at medium initial voltage values (see Fig. F.16(b) for voltage distributions in the moderately nonlinear regime). The slight decrease in the IPRs near $\psi_0 = 0$ is attributed to a mismatch between the initial excitation and the established soliton shape (see further details in Appendix G). Additionally, the overall reduction in the experimentally measured IPRs is due to the circuit dissipation. Nonetheless, the consistent localization-delocalization-localization transition, which is revealed by the experimental measurements and theoretical prediction alike, confirms that one type of the bulk solitons occu-

pies the middle finite bandgap under the action of weak nonlinearity, while the other type emerges in the semi-infinite gap under strong nonlinearity. As expected, no localized solitons are found in the system with medium nonlinearity strength. Figure H.18 illustrates this transition, and Appendix H provides a relevant discussion.

3. Discussion

It is relevant to summarize unique phenomena exhibited by the NLQTI proposed and implemented in the present work. First, in the nonlinear Wannier-type HOTI proposed in Ref. [72], localized states arise solely as nonlinearity-induced topological corner states. In contrast, our NLQTI demonstrates the nonlinearity-controlled localization-delocalization-localization transition, allowing the setup to switch between the nonlinear topological corner states and topologically trivial corner solitons. Second, in the nonlinear Wannier-type HOTIs, corner states are inherently coupled to the edge modes [73] or to bulk states when the lattice exhibits weak dimerization [74]. Conversely, the corner states in QTIs are sharply separated from other states, admitting the existence of the well-localized nonlinear corner states and bulk solitons, even when the lattice dimerization is weak (see further details in Appendix I).

Thus, we have introduced the concept of NLQTIs and demonstrated their experimental realization in an electric-circuit lattice. Through the quench dynamics, we have observed the nonlinear topological corner states and topologically trivial corner solitons in the weakly and strongly nonlinear regimes, respectively. Further, this work reveals the formation of two distinct types of the bulk solitons: one type exists in the middle finite bandgap under the action of weak nonlinearity, while the other one populates the semi-infinite gap under strong nonlinearity. Eventually, the present work reports the advancement in the studies of nonlinear HOTIs, establishing another member of the nonlinear HOTI family and suggesting new avenues for exploring novel solitons across a broad range of TIs.

CRediT authorship contribution statement

Ruijiang Li: Conceptualization, Data curation, Formal analysis, Funding acquisition, Investigation, Methodology, Project administration, Resources, Software, Supervision, Validation, Visualization, Writing – original draft, Writing – review & editing. **Wencai Wang:** Investigation, Visualization. **Yongtao Jia:** Resources. **Ying Liu:** Funding acquisition, Project administration, Resources. **Pengfei Li:** Formal analysis, Methodology. **Boris A. Malomed:** Formal analysis, Supervision, Writing – review & editing.

Declaration of competing interest

The authors declare that they have no known competing financial interests or personal relationships that could have appeared to influence the work reported in this paper.

Data availability

Data will be made available on request.

Acknowledgements

The authors would like to thank Haoran Xue and Jian-Hua Jiang for fruitful discussions. R.L. and W.W. were sponsored by the National Key Research and Development Program of China (Grant No. 2022YFA1404902), National Natural Science Foundation of China (Grant No. 12104353), and Fundamental Research Funds for the Central Universities (Grant No. QTZX25086). Y.L. was sponsored by the National Natural Science Foundation of China (NSFC) under Grant No. 62271366 and the 111 Project. P.L. was sponsored by the National Natural Science Foundation of China (11805141) and Basic Research Program of Shanxi Provence (202303021211185). The work of B.A.M. was supported, in part, by the Israel Science Foundation through grant No. 1695/22. Numerical calculations performed in this work were supported by the High-Performance Computing Platform of Xidian University.

Appendix A. The model of the interacting bosonic gas

In this section, we construct the model for the interacting boson gas and demonstrate that it effectively emulates the NLQTI. We consider a gas of identical bosons hopping on a two-dimensional (2D) lattice. The respective Hamiltonian,

$$\hat{H} = \hat{H}_{\text{kin}} + \hat{H}_{\text{int}}, \quad (\text{A.1})$$

includes the kinetic term,

$$\begin{aligned} \hat{H}_{\text{kin}} = & \sum_{m,n} \left[\gamma \left(c_{m,n}^{(1)\dagger} c_{m,n}^{(3)} + c_{m,n}^{(2)\dagger} c_{m,n}^{(4)} + \text{H.c.} \right) \right. \\ & + \gamma \left(c_{m,n}^{(1)\dagger} c_{m,n}^{(4)} - c_{m,n}^{(2)\dagger} c_{m,n}^{(3)} + \text{H.c.} \right) \\ & + \lambda \left(c_{m,n}^{(1)\dagger} c_{m+1,n}^{(3)} + c_{m,n}^{(4)\dagger} c_{m+1,n}^{(2)} + \text{H.c.} \right) \\ & \left. + \lambda \left(c_{m,n}^{(1)\dagger} c_{m,n+1}^{(4)} - c_{m,n}^{(3)\dagger} c_{m,n+1}^{(2)} + \text{H.c.} \right) \right. \\ & \left. + \sum_j \delta_j c_{m,n}^{(j)\dagger} c_{m,n}^{(j)} \right], \end{aligned} \quad (\text{A.2})$$

where H.c. stands for the Hermite conjugate expression, $c_{m,n}^{(j)\dagger}$ and $c_{m,n}^{(j)}$ are the bosonic creation and annihilation operators, respectively, at site j in the unit cell (m, n) , with $j = 1, 2, 3, 4$, which obey the canonical commutation relations:

$$\left[c_{m,n}^{(j)}, c_{m',n'}^{(j')\dagger} \right] = \delta_{m,m'} \delta_{n,n'} \delta_{j,j'}. \quad (\text{A.3})$$

Here, γ is the hopping amplitude for particles between adjacent sites in the same unit cell, while λ is the amplitude of hopping between nearest-neighbor unit cells. The negative signs in Eq. (A.2) correspond to the gauge choice which implies the π -flux threading through a plaquette (including the unit cell itself). Further, δ_j with $j = 1, 2, 3, 4$ represent the energy offsets

between sites within one unit cell. The interaction Hamiltonian in Eq. (3) represents the onsite interactions between particles:

$$\hat{H}_{\text{int}} = \frac{g}{2} \sum_{m,n,j} \hat{n}_{m,n}^{(j)} (\hat{n}_{m,n}^{(j)} - 1), \quad (\text{A.4})$$

where $\hat{n}_{m,n}^{(j)}$ is the number operator counting the bosons at site j in unit cell (m, n) , and g is the strength of the onsite interaction between the particles, while we neglect the interaction between particles on different sites. Using the commutation relations, the interaction Hamiltonian can be rewritten as:

$$\hat{H}_{\text{int}} = \frac{g}{2} \sum_{m,n,j} c_{m,n}^{(j)\dagger} c_{m,n}^{(j)\dagger} c_{m,n}^{(j)} c_{m,n}^{(j)}. \quad (\text{A.5})$$

Solving the many-body interacting problem for Hamiltonian \hat{H} from Eq. (3) is a challenging task. In the mean-field approximation, the macroscopic state, i.e., $|\Phi\rangle$, is chosen as the tensor product of Glauber coherent states $|\Phi\rangle = \otimes_{m,n,j} |\psi_{m,n}^{(j)}\rangle_{\text{GCS}}$, where $|\psi_{m,n}^{(j)}\rangle_{\text{GCS}}$ describes only a single site and it is an eigenstate of the annihilation operator with $c_{m,n}^{(j)} |\psi_{m,n}^{(j)}\rangle_{\text{GCS}} = \psi_{m,n}^{(j)} |\psi_{m,n}^{(j)}\rangle_{\text{GCS}}$ [83]. With $H = \langle \Phi | \hat{H} | \Phi \rangle$, the respective semi-classical Hamiltonian can be written as:

$$\begin{aligned} H = & \sum_{m,n} \left[\gamma \left(\psi_{m,n}^{(1)*} \psi_{m,n}^{(3)} + \psi_{m,n}^{(2)*} \psi_{m,n}^{(4)} + \psi_{m,n}^{(3)*} \psi_{m,n}^{(1)} + \psi_{m,n}^{(4)*} \psi_{m,n}^{(2)} \right) \right. \\ & + \gamma \left(\psi_{m,n}^{(1)*} \psi_{m,n}^{(4)} - \psi_{m,n}^{(2)*} \psi_{m,n}^{(3)} + \psi_{m,n}^{(4)*} \psi_{m,n}^{(1)} - \psi_{m,n}^{(3)*} \psi_{m,n}^{(2)} \right) \\ & + \lambda \left(\psi_{m,n}^{(1)*} \psi_{m+1,n}^{(3)} + \psi_{m,n}^{(4)*} \psi_{m+1,n}^{(2)} + \psi_{m+1,n}^{(3)*} \psi_{m,n}^{(1)} + \psi_{m+1,n}^{(2)*} \psi_{m,n}^{(4)} \right) \\ & + \lambda \left(\psi_{m,n}^{(1)*} \psi_{m,n+1}^{(4)} - \psi_{m,n}^{(3)*} \psi_{m,n+1}^{(2)} + \psi_{m,n+1}^{(4)*} \psi_{m,n}^{(1)} - \psi_{m,n+1}^{(2)*} \psi_{m,n}^{(3)} \right) \\ & + \sum_j \delta_j |\psi_{m,n}^{(j)}|^2 \\ & \left. + \frac{g}{2} \left(|\psi_{m,n}^{(1)}|^4 + |\psi_{m,n}^{(2)}|^4 + |\psi_{m,n}^{(3)}|^4 + |\psi_{m,n}^{(4)}|^4 \right) \right]. \end{aligned} \quad (\text{A.6})$$

By rearranging the terms in the above expression, this Hamiltonian can be rewritten as:

$$\begin{aligned} H = & \sum_{m,n} \left[\left(\gamma \psi_{m,n}^{(3)} + \gamma \psi_{m,n}^{(4)} + \lambda \psi_{m+1,n}^{(3)} + \lambda \psi_{m,n+1}^{(4)} \right) \psi_{m,n}^{(1)*} \right. \\ & + \left(-\gamma \psi_{m,n}^{(3)} + \gamma \psi_{m,n}^{(4)} + \lambda \psi_{m-1,n}^{(4)} - \lambda \psi_{m,n-1}^{(3)} \right) \psi_{m,n}^{(2)*} \\ & + \left(\gamma \psi_{m,n}^{(1)} - \gamma \psi_{m,n}^{(2)} + \lambda \psi_{m-1,n}^{(1)} - \lambda \psi_{m,n+1}^{(2)} \right) \psi_{m,n}^{(3)*} \\ & + \left(\gamma \psi_{m,n}^{(1)} + \gamma \psi_{m,n}^{(2)} + \lambda \psi_{m+1,n}^{(2)} + \lambda \psi_{m,n-1}^{(1)} \right) \psi_{m,n}^{(4)*} \\ & + \sum_j \delta_j |\psi_{m,n}^{(j)}|^2 \\ & \left. + \frac{g}{2} \left(|\psi_{m,n}^{(1)}|^4 + |\psi_{m,n}^{(2)}|^4 + |\psi_{m,n}^{(3)}|^4 + |\psi_{m,n}^{(4)}|^4 \right) \right]. \end{aligned} \quad (\text{A.7})$$

The respective equations of motion,

$$i \frac{d\psi_{m,n}^{(j)}}{dt} = \frac{\delta H}{\delta \psi_{m,n}^{(j)*}}, \quad j = 1, 2, 3, 4, \quad (\text{A.8})$$

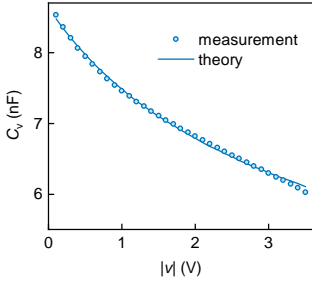


Figure B.4: The capacitance-voltage relation of two parallel-connected common-cathode diodes. The curve represents theoretical results, while the circular points correspond to data of the experimental measurements.

derived from Hamiltonian (A.7), take the following form:

$$i \frac{d\psi_{m,n}^{(1)}}{dt} = \delta_1 \psi_{m,n}^{(1)} + \gamma \psi_{m,n}^{(3)} + \gamma \psi_{m,n}^{(4)} + \lambda \psi_{m+1,n}^{(3)} + \lambda \psi_{m,n+1}^{(4)} + g |\psi_{m,n}^{(1)}|^2 \psi_{m,n}^{(1)}, \quad (\text{A.9})$$

$$i \frac{d\psi_{m,n}^{(2)}}{dt} = \delta_2 \psi_{m,n}^{(2)} + \gamma \psi_{m,n}^{(4)} - \gamma \psi_{m,n}^{(3)} + \lambda \psi_{m-1,n}^{(4)} - \lambda \psi_{m,n-1}^{(3)} + g |\psi_{m,n}^{(2)}|^2 \psi_{m,n}^{(2)}, \quad (\text{A.10})$$

$$i \frac{d\psi_{m,n}^{(3)}}{dt} = \delta_3 \psi_{m,n}^{(3)} + \gamma \psi_{m,n}^{(1)} - \gamma \psi_{m,n}^{(2)} + \lambda \psi_{m-1,n}^{(1)} - \lambda \psi_{m,n+1}^{(2)} + g |\psi_{m,n}^{(3)}|^2 \psi_{m,n}^{(3)}, \quad (\text{A.11})$$

$$i \frac{d\psi_{m,n}^{(4)}}{dt} = \delta_4 \psi_{m,n}^{(4)} + \gamma \psi_{m,n}^{(2)} + \gamma \psi_{m,n}^{(1)} + \lambda \psi_{m+1,n}^{(2)} + \lambda \psi_{m,n-1}^{(1)} + g |\psi_{m,n}^{(4)}|^2 \psi_{m,n}^{(4)}. \quad (\text{A.12})$$

Setting $\delta_1 = \delta_2 = \delta_3 = \delta_4$, these equations describe the NLQTI, where the usual onsite energies, corresponding to the cubic nonlinearity, are quadratic functions of the amplitudes at the corresponding sites.

Appendix B. The derivation of circuit equations for the nonlinear quadrupole topological insulator

This section is organized as follows. In the first subsection, we introduce a model with the common-cathode diodes. Then, in the second subsection, we derive the circuit equations which take the form as the governing equations of the NLQTI.

Appendix B.1. The model with common-cathode diodes

We utilize two parallel-connected common-cathode diodes (V60DM45C) as the onsite nonlinearity for the NLQTI. These diodes are mounted on the top and bottom layers of the PCB, respectively. Similar to back-to-back varactor diodes, the use of common-cathode diodes ensures identical responses in the course of the two half-cycles of the AC voltage, eliminating the need for a bias voltage [84]. Although the capacitance of the common-cathode diodes is time-dependent, our simulations and experimental measurements show that the high-harmonic currents induced by the diodes are negligible. Therefore, the

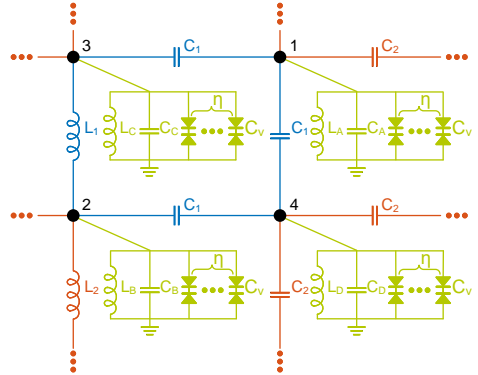


Figure B.5: A schematic of the NLQTI realized in the circuit lattice. For the clarity's sake, only the unit cell is shown.

capacitance of the common-cathode diodes can be expressed as:

$$C = i \frac{j_v}{\omega v}, \quad (\text{B.1})$$

where j_v and v represent the amplitudes of the current and voltage, respectively, and ω is the angular frequency of the applied voltage signal. After obtaining the experimental data for the capacitance-voltage relation of two parallel-connected common-cathode diodes, we fit the capacitance-voltage curve to expression (1) in the main text, i.e.,

$$C(v) = \frac{C_L}{(1 + |v/v_0|)^M}, \quad (\text{B.2})$$

where C_L is the capacitance at zero voltage, v_0 and M are constants, and v represents the amplitude of the applied voltage. Figure B.4 shows the capacitance-voltage relation of two parallel-connected common-cathode diodes, with the curve representing the theoretical results and the circular points corresponding to the experimental data. The adopted parameters of the parallel-connected common-cathode diodes are $C_L = 8.6$ nF, $v_0 = 1.7$, and $M = 0.3$. Thus, the common-cathode diodes function as variable capacitors, with the capacitance depending on the voltage amplitude. We have also performed experimental measurements of the common-cathode diodes at other frequencies, concluding that Eq. (B.2) remains valid across the entire parameter range of our study. Extending this conclusion, when the applied voltage is quasi-monochromatic with $V(t) = \frac{1}{2}v(t)e^{-i\omega t} + \text{c.c.}$, the capacitance of the common-cathode diodes can be written as

$$C(v) = \frac{C_L}{[1 + |v(t)/v_0|]^M}, \quad (\text{B.3})$$

where $v(t)$ is the slowly-varying envelope amplitude. In this case, the capacitance of the common-cathode diodes varies with the voltage envelope.

Appendix B.2. The derivation of circuit equations

We aim to build a generic circuit lattice emulating the NLQTI. As shown in Fig. B.5, the system is built of nonlinear oscillators composed of inductors $L_{A,B,C,D}$, capacitors

$C_{A,B,C,D}$, and common-cathode diodes with capacitance C_v . To enhance the nonlinear response, each oscillator includes J parallel-connected common-cathode diodes (i.e., the number of common-cathode diodes is J). The oscillators are interconnected by coupling elements C_1 , C_2 , L_1 , and L_2 . The common-cathode diode acts as a voltage-dependent capacitor, with the total capacitance $C_v = C_L + C_{NL}$, where C_L and C_{NL} are the linear and nonlinear terms, respectively. The linear part C_L is constant, while for the time-harmonic voltage $V(t) = \frac{1}{2}ve^{-i\omega t} + \text{c.c.}$, the nonlinear component is $C_{NL} = -C_L + \frac{C_L}{(1+|v/v_0|)^M}$, with constant parameters v_0 and M (cf. Eq. (B.3)). The grounding capacitance and inductance satisfy relations

$$C_{A,B,C,D} = C_g + \Delta C_{A,B,C,D} \quad (\text{B.4})$$

and

$$\frac{1}{L_{A,B,C,D}} = \frac{1}{L_g} + \frac{1}{\Delta L_{A,B,C,D}}, \quad (\text{B.5})$$

respectively.

Usually, the differences between C_A , C_B , C_C , and C_D are small, and the nonlinear component of the diode capacitance, C_{NL} , is small too. Therefore, the total grounding capacitance may be approximated as $C_g + JC_L$. Similarly, the differences between L_A , L_B , L_C , and L_D are also small. Given that $C_g + JC_L \gg C_{1,2}$ and $L_g \ll L_{1,2}$, the voltages at the circuit nodes can be expressed as $V(t) = \frac{1}{2}v(t)e^{-i\omega_0 t} + \text{c.c.}$, where $v(t)$ is the slowly-varying complex amplitude and

$$\omega_0 = \frac{1}{\sqrt{L_g(C_g + JC_L)}} \quad (\text{B.6})$$

is the carrier frequency. Accordingly, the nonlinear component of the diode capacitance is given by

$$C_{NL} = -C_L + \frac{C_L}{[1 + |v(t)/v_0|]^M}. \quad (\text{B.7})$$

For the four circuit nodes in the (m, n) -th unit cell, the following relations can be obtained using the Kirchhoff's law:

$$\begin{aligned} & C_1 \frac{d^2 V_{m,n}^{(3)}}{dt^2} + C_2 \frac{d^2 V_{m+1,n}^{(3)}}{dt^2} + C_1 \frac{d^2 V_{m,n}^{(4)}}{dt^2} + C_2 \frac{d^2 V_{m,n+1}^{(4)}}{dt^2} \\ & - [\Delta C_A + 2C_1 + 2C_2 + JC_{NL}(v_{m,n}^{(1)})] \frac{d^2 V_{m,n}^{(1)}}{dt^2} - \frac{V_{m,n}^{(1)}}{\Delta L_A} \\ & = \frac{V_{m,n}^{(1)}}{L_g} + (C_g + JC_L) \frac{d^2 V_{m,n}^{(1)}}{dt^2}, \end{aligned} \quad (\text{B.8})$$

$$\begin{aligned} & C_2 \frac{d^2 V_{m-1,n}^{(4)}}{dt^2} + C_1 \frac{d^2 V_{m,n}^{(4)}}{dt^2} + \frac{V_{m,n}^{(3)}}{L_1} + \frac{V_{m,n-1}^{(3)}}{L_2} \\ & - [\Delta C_B + C_1 + C_2 + JC_{NL}(v_{m,n}^{(2)})] \frac{d^2 V_{m,n}^{(2)}}{dt^2} \\ & - \left(\frac{1}{\Delta L_B} + \frac{1}{L_1} + \frac{1}{L_2} \right) V_{m,n}^{(2)} \\ & = \frac{V_{m,n}^{(2)}}{L_g} + (C_g + JC_L) \frac{d^2 V_{m,n}^{(2)}}{dt^2}, \end{aligned} \quad (\text{B.9})$$

$$\begin{aligned} & C_2 \frac{d^2 V_{m-1,n}^{(1)}}{dt^2} + C_1 \frac{d^2 V_{m,n}^{(1)}}{dt^2} + \frac{1}{L_1} V_{m,n}^{(2)} + \frac{1}{L_2} V_{m,n+1}^{(2)} \\ & - [\Delta C_C + C_1 + C_2 + JC_{NL}(v_{m,n}^{(3)})] \frac{d^2 V_{m,n}^{(3)}}{dt^2} \\ & - \left(\frac{1}{\Delta L_C} + \frac{1}{L_1} + \frac{1}{L_2} \right) V_{m,n}^{(3)} \\ & = \frac{V_{m,n}^{(3)}}{L_g} + (C_g + JC_L) \frac{d^2 V_{m,n}^{(3)}}{dt^2}, \end{aligned} \quad (\text{B.10})$$

$$\begin{aligned} & C_1 \frac{d^2 V_{m,n}^{(2)}}{dt^2} + C_2 \frac{d^2 V_{m+1,n}^{(2)}}{dt^2} + C_2 \frac{d^2 V_{m,n-1}^{(1)}}{dt^2} + C_1 \frac{d^2 V_{m,n}^{(1)}}{dt^2} \\ & - [\Delta C_D + 2C_1 + 2C_2 + JC_{NL}(v_{m,n}^{(4)})] \frac{d^2 V_{m,n}^{(4)}}{dt^2} - \frac{V_{m,n}^{(4)}}{\Delta L_D} \\ & = \frac{V_{m,n}^{(4)}}{L_g} + (C_g + JC_L) \frac{d^2 V_{m,n}^{(4)}}{dt^2}, \end{aligned} \quad (\text{B.11})$$

where the linear and nonlinear components of the diode capacitance have been separated. These equations describe the time-dependent voltage distribution across the circuit lattice.

The voltages at each circuit node can be expressed as $V_{m,n}^{(1,2,3,4)} = \frac{1}{2}v_{m,n}^{(1,2,3,4)}e^{-i\omega_0 t} + \text{c.c.}$, from which we can obtain the first and second derivatives. Due to relations $C_g + JC_L \gg C_{1,2}$, C_{NL} , $\Delta C_{A,B,C,D}$ and $L_g \ll L_{1,2}$, we apply the slowly-varying-envelope approximation. In Eqs. (B.8)-(B.11), we use

$$\frac{d^2 V_{m,n}^{(1,2,3,4)}}{dt^2} = -i\omega_0 \frac{dv_{m,n}^{(1,2,3,4)}}{dt} e^{-i\omega_0 t} - \frac{\omega_0^2}{2} v_{m,n}^{(1,2,3,4)} e^{-i\omega_0 t} + \text{c.c.} \quad (\text{B.12})$$

for the terms on the right-hand side. For the other terms, we instead use

$$\frac{d^2 V_{m,n}^{(1,2,3,4)}}{dt^2} = -\frac{\omega_0^2}{2} v_{m,n}^{(1,2,3,4)} e^{-i\omega_0 t} + \text{c.c.} \quad (\text{B.13})$$

Thus, Eqs. (B.8)-(B.11) are reduced to

$$\begin{aligned} i \frac{dv_{m,n}^{(1)}}{dt} &= \left[-\frac{2C_1 + 2C_2 + \Delta C_A + JC_{NL}(v_{m,n}^{(1)})}{2(C_g + JC_L)} + \frac{L_g}{2} \frac{1}{\Delta L_A} \right] \omega_0 v_{m,n}^{(1)} \\ &+ \frac{C_1}{2(C_g + JC_L)} \omega_0 v_{m,n}^{(3)} + \frac{C_2}{2(C_g + JC_L)} \omega_0 v_{m+1,n}^{(3)} \\ &+ \frac{C_1}{2(C_g + JC_L)} \omega_0 v_{m,n}^{(4)} + \frac{C_2}{2(C_g + JC_L)} \omega_0 v_{m,n+1}^{(4)}, \end{aligned} \quad (\text{B.14})$$

$$\begin{aligned} i \frac{dv_{m,n}^{(2)}}{dt} &= \left[-\frac{C_1 + C_2 + \Delta C_B + JC_{NL}(v_{m,n}^{(2)})}{2(C_g + JC_L)} \right] \omega_0 v_{m,n}^{(2)} \\ &+ \left[\frac{L_g}{2} \left(\frac{1}{L_1} + \frac{1}{L_2} + \frac{1}{\Delta L_B} \right) \right] \omega_0 v_{m,n}^{(2)} \\ &- \frac{L_g}{2L_1} \omega_0 v_{m,n}^{(3)} - \frac{L_g}{2L_2} \omega_0 v_{m,n-1}^{(3)} \\ &+ \frac{C_1}{2(C_g + JC_L)} \omega_0 v_{m,n}^{(4)} + \frac{C_2}{2(C_g + JC_L)} \omega_0 v_{m-1,n}^{(4)}, \end{aligned} \quad (\text{B.15})$$

$$\begin{aligned} i \frac{dv_{m,n}^{(3)}}{dt} = & \left[-\frac{C_1 + C_2 + \Delta C_C + JC_{NL}(v_{m,n}^{(3)})}{2(C_g + JC_L)} \right] \omega_0 v_{m,n}^{(3)} \\ & + \left[\frac{L_g}{2} \left(\frac{1}{L_1} + \frac{1}{L_2} + \frac{1}{\Delta L_C} \right) \right] \omega_0 v_{m,n}^{(3)} \\ & - \frac{L_g}{2L_1} \omega_0 v_{m,n}^{(2)} - \frac{L_g}{2L_2} \omega_0 v_{m,n+1}^{(2)} \\ & + \frac{C_1}{2(C_g + JC_L)} \omega_0 v_{m,n}^{(1)} + \frac{C_2}{2(C_g + JC_L)} \omega_0 v_{m-1,n}^{(1)}, \quad (B.16) \end{aligned}$$

$$\begin{aligned} i \frac{dv_{m,n}^{(4)}}{dt} = & \left[-\frac{2C_1 + 2C_2 + \Delta C_D + JC_{NL}(v_{m,n}^{(4)})}{2(C_g + JC_L)} + \frac{L_g}{2} \frac{1}{\Delta L_D} \right] \omega_0 v_{m,n}^{(4)} \\ & + \frac{C_1}{2(C_g + JC_L)} \omega_0 v_{m,n}^{(1)} + \frac{C_2}{2(C_g + JC_L)} \omega_0 v_{m,n-1}^{(1)} \\ & + \frac{C_1}{2(C_g + JC_L)} \omega_0 v_{m,n}^{(2)} + \frac{C_2}{2(C_g + JC_L)} \omega_0 v_{m+1,n}^{(2)}. \quad (B.17) \end{aligned}$$

We define $v_{m,n}^{(1,2,3,4)}(t) = V_{m,n}^{(1,2,3,4)}(t) \exp(i\omega_0 t)$, and, for the simplicity's sake, we also define $T = \omega_n t$, where ω_n is the normalized frequency. Then, the equations can be naturally written as

$$\begin{aligned} i \frac{dV_{m,n}^{(1)}}{dT} = & \delta_1 V_{m,n}^{(1)} + \gamma_C V_{m,n}^{(3)} + \lambda_C V_{m+1,n}^{(3)} + \gamma_C V_{m,n}^{(4)} + \lambda_C V_{m,n+1}^{(4)} \\ & + g(V_{m,n}^{(1)}) V_{m,n}^{(1)}, \quad (B.18) \end{aligned}$$

$$\begin{aligned} i \frac{dV_{m,n}^{(2)}}{dT} = & \delta_2 V_{m,n}^{(2)} - \gamma_L V_{m,n}^{(3)} - \lambda_L V_{m,n-1}^{(3)} + \gamma_C V_{m,n}^{(4)} + \lambda_C V_{m-1,n}^{(4)} \\ & + g(V_{m,n}^{(2)}) V_{m,n}^{(2)}, \quad (B.19) \end{aligned}$$

$$\begin{aligned} i \frac{dV_{m,n}^{(3)}}{dT} = & \delta_3 V_{m,n}^{(3)} - \gamma_L V_{m,n}^{(2)} - \lambda_L V_{m,n+1}^{(2)} + \gamma_C V_{m,n}^{(1)} + \lambda_C V_{m-1,n}^{(1)} \\ & + g(V_{m,n}^{(3)}) V_{m,n}^{(3)}, \quad (B.20) \end{aligned}$$

$$\begin{aligned} i \frac{dV_{m,n}^{(4)}}{dT} = & \delta_4 V_{m,n}^{(4)} + \gamma_C V_{m,n}^{(1)} + \lambda_C V_{m,n-1}^{(1)} + \gamma_C V_{m,n}^{(2)} + \lambda_C V_{m+1,n}^{(2)} \\ & + g(V_{m,n}^{(4)}) V_{m,n}^{(4)}, \quad (B.21) \end{aligned}$$

where

$$\delta_1 = \frac{\omega_0}{\omega_n} - \frac{2C_1 + 2C_2 + \Delta C_A}{2(C_g + JC_L)} \frac{\omega_0}{\omega_n} + \frac{L_g}{2} \frac{1}{\Delta L_A} \frac{\omega_0}{\omega_n}, \quad (B.22)$$

$$\begin{aligned} \delta_2 = & \frac{\omega_0}{\omega_n} - \frac{C_1 + C_2 + \Delta C_B}{2(C_g + JC_L)} \frac{\omega_0}{\omega_n} \\ & + \frac{L_g}{2} \left(\frac{1}{L_1} + \frac{1}{L_2} + \frac{1}{\Delta L_B} \right) \frac{\omega_0}{\omega_n}, \quad (B.23) \end{aligned}$$

$$\begin{aligned} \delta_3 = & \frac{\omega_0}{\omega_n} - \frac{C_1 + C_2 + \Delta C_C}{2(C_g + JC_L)} \frac{\omega_0}{\omega_n} \\ & + \frac{L_g}{2} \left(\frac{1}{L_1} + \frac{1}{L_2} + \frac{1}{\Delta L_C} \right) \frac{\omega_0}{\omega_n}, \quad (B.24) \end{aligned}$$

$$\delta_4 = \frac{\omega_0}{\omega_n} - \frac{2C_1 + 2C_2 + \Delta C_D}{2(C_g + JC_L)} \frac{\omega_0}{\omega_n} + \frac{L_g}{2\Delta L_D} \frac{\omega_0}{\omega_n}, \quad (B.25)$$

represent the constant onsite energies,

$$\gamma_C = \frac{C_1}{2(C_g + JC_L)} \frac{\omega_0}{\omega_n}, \quad (B.26)$$

$$\lambda_C = \frac{C_2}{2(C_g + JC_L)} \frac{\omega_0}{\omega_n}, \quad (B.27)$$

$$\gamma_L = \frac{L_g}{2L_1} \frac{\omega_0}{\omega_n}, \quad (B.28)$$

$$\lambda_L = \frac{L_g}{2L_2} \frac{\omega_0}{\omega_n}, \quad (B.29)$$

represent the hopping strengths, and

$$g(V_{m,n}^{(1,2,3,4)}) = -\frac{JC_{NL}(V_{m,n}^{(1,2,3,4)})}{2(C_g + JC_L)} \frac{\omega_0}{\omega_n} \quad (B.30)$$

determines the amplitude-dependent onsite energies. These equations govern the evolution in the circuit lattice.

To emulate the NLQTI, the coefficients must satisfy constraints $\delta_1 = \delta_2 = \delta_3 = \delta_4 \equiv \delta$, $\gamma_C = \gamma_L \equiv \gamma$, and $\lambda_C = \lambda_L \equiv \lambda$. To find the most basic NLQTI states, we also set $\Delta C_A = \Delta C_D = 0$, $\Delta C_B = \Delta C_C = C_1 + C_2$, $\frac{1}{\Delta L_B} = \frac{1}{\Delta L_C} = 0$, and $\frac{1}{\Delta L_A} = \frac{1}{\Delta L_D} = \frac{1}{L_1} + \frac{1}{L_2}$, which leads to the following relations between the circuit parameters:

$$C_A = C_D = C_g, \quad (B.31)$$

$$L_B = L_C = L_g, \quad (B.32)$$

$$C_B = C_C = C_g + C_1 + C_2, \quad (B.33)$$

$$\frac{1}{L_A} = \frac{1}{L_D} = \frac{1}{L_g} + \frac{1}{L_1} + \frac{1}{L_2}, \quad (B.34)$$

$$C_1 = \frac{L_g(C_g + JC_L)}{L_1}, \quad (B.35)$$

$$C_2 = \frac{L_g(C_g + JC_L)}{L_2}. \quad (B.36)$$

Appendix C. The consideration on the linear quadrupole topological insulator (QTI)

In this section, we demonstrate how the model of the NLQTI can be reduced to its linear counterpart, which corresponds exactly to the seminal lattice model for the linear QTI [3].

In the linear limit, where $C_{NL} = 0$, Eqs. (B.18)-(B.21) reduce to the following equations:

$$\begin{aligned} i \frac{dV_{m,n}^{(1)}}{dT} = & \delta_1 V_{m,n}^{(1)} + \gamma_C V_{m,n}^{(3)} + \lambda_C V_{m+1,n}^{(3)} + \gamma_C V_{m,n}^{(4)} \\ & + \lambda_C V_{m,n+1}^{(4)}, \quad (C.1) \end{aligned}$$

$$\begin{aligned} i \frac{dV_{m,n}^{(2)}}{dT} = & \delta_2 V_{m,n}^{(2)} - \gamma_L V_{m,n}^{(3)} - \lambda_L V_{m,n-1}^{(3)} + \gamma_C V_{m,n}^{(4)} \\ & + \lambda_C V_{m-1,n}^{(4)}, \quad (C.2) \end{aligned}$$

$$\begin{aligned} i \frac{dV_{m,n}^{(3)}}{dT} = & \delta_3 V_{m,n}^{(3)} - \gamma_L V_{m,n}^{(2)} - \lambda_L V_{m,n+1}^{(2)} + \gamma_C V_{m,n}^{(1)} \\ & + \lambda_C V_{m-1,n}^{(1)}, \quad (C.3) \end{aligned}$$

$$\begin{aligned} i \frac{dV_{m,n}^{(4)}}{dT} = & \delta_4 V_{m,n}^{(4)} + \gamma_C V_{m,n}^{(1)} + \lambda_C V_{m,n-1}^{(1)} + \gamma_C V_{m,n}^{(2)} \\ & + \lambda_C V_{m+1,n}^{(2)}, \quad (C.4) \end{aligned}$$

where $\delta_{1,2,3,4}$, $\gamma_{C,L}$, and $\lambda_{C,L}$ retain the same form as defined in Eqs. (B.22)-(B.29). To establish the correspondence between our circuit model and the tight-binding one proposed in Ref. [3], the coefficients are subject to constraints $\delta_1 = \delta_2 = \delta_3 = \delta_4 \equiv \delta$, $\gamma_C = \gamma_L \equiv \gamma$, and $\lambda_C = \lambda_L \equiv \lambda$. We define the circuit parameters in the same way as those in Eqs. (B.31)-(B.36), which reduce to

$$i \frac{dV_{m,n}^{(1)}}{dT} = \delta V_{m,n}^{(1)} + \gamma V_{m,n}^{(3)} + \lambda V_{m+1,n}^{(3)} + \gamma V_{m,n}^{(4)} + \lambda V_{m,n+1}^{(4)}, \quad (C.5)$$

$$i \frac{dV_{m,n}^{(2)}}{dT} = \delta V_{m,n}^{(2)} - \gamma V_{m,n}^{(3)} - \lambda V_{m,n-1}^{(3)} + \gamma V_{m,n}^{(4)} + \lambda V_{m-1,n}^{(4)}, \quad (C.6)$$

$$i \frac{dV_{m,n}^{(3)}}{dT} = \delta V_{m,n}^{(3)} - \gamma V_{m,n}^{(2)} - \lambda V_{m,n+1}^{(2)} + \gamma V_{m,n}^{(1)} + \lambda V_{m-1,n}^{(1)}, \quad (C.7)$$

$$i \frac{dV_{m,n}^{(4)}}{dT} = \delta V_{m,n}^{(4)} + \gamma V_{m,n}^{(1)} + \lambda V_{m,n-1}^{(1)} + \gamma V_{m,n}^{(2)} + \lambda V_{m+1,n}^{(2)}. \quad (C.8)$$

For the linear QTI with periodic boundary conditions in the x and y directions, the respective Hamiltonian in the k -space can be written as

$$H = (\gamma + \lambda \cos k_x) \Gamma_4 + \lambda \sin k_x \Gamma_3 + (\gamma + \lambda \cos k_y) \Gamma_2 + \lambda \sin k_y \Gamma_1 + \delta \Gamma_0, \quad (C.9)$$

where $\Gamma_0 = \tau_0 \sigma_0$, $\Gamma_1 = -\tau_2 \sigma_1$, $\Gamma_2 = -\tau_2 \sigma_2$, $\Gamma_3 = -\tau_2 \sigma_3$, and $\Gamma_4 = \tau_1 \sigma_0$, with τ and σ being two sets of the Pauli matrices (τ_0 and σ_0 stand for the unit matrix). The corresponding eigenfrequencies are given by

$$\bar{\omega} = \delta \pm \sqrt{2\gamma^2 + 2\lambda^2 + 2\gamma\lambda(\cos k_x + \cos k_y)}. \quad (C.10)$$

Both the upper and lower energy bands are twofold degenerate. A frequency gap (equivalent to the energy gap in Ref. [3]) exists unless $|\gamma/\lambda| = 1$. Accordingly, the phase transition occurs at $\gamma/\lambda = 1$ ($\gamma/\lambda = -1$), with the corresponding bulk frequency gap closing at the $\mathbf{M} = (\pi, \pi)$ ($\Gamma = (0, 0)$) point of the Brillouin zone [3]. When $|\gamma/\lambda| \neq 1$, the size of the bandgap, according to Eq. (C.10), is $2\sqrt{2}|\gamma - \lambda|$ when γ and λ have the same sign, and by $2\sqrt{2}|\gamma + \lambda|$ when γ and λ have different signs. Finally, the bands become flat when $\gamma = 0$ or $\lambda = 0$.

The linear QTI exhibits several symmetry properties [3]. First, the system maintains reflection symmetries, as the Hamiltonian satisfies the relation

$$m_j H(k) m_j^\dagger = H(M_j k), \quad (C.11)$$

for $j = x, y$, where $m_x = \tau_1 \sigma_3$, $m_y = \tau_1 \sigma_1$, with $M_x(k_x, k_y) = (-k_x, k_y)$ and $M_y(k_x, k_y) = (k_x, -k_y)$. Both reflection symmetries hold for the present lattice model. Note that matrices m_x and m_y do not commute; instead, they anticommute, so that $\{m_x, m_y\} = 0$ in the present model. Second, the model also maintains the time-reversal symmetry, with $T = K$ as the time-reversal operator. Here, K is the complex-conjugation operator. In the coordinate space, this symmetry requires that

$$THT^{-1} = H, \quad (C.12)$$

where $T = T^{-1} = K$. The latter condition reduces to $H^* = H$, meaning that the Hamiltonian is real in the coordinate space,

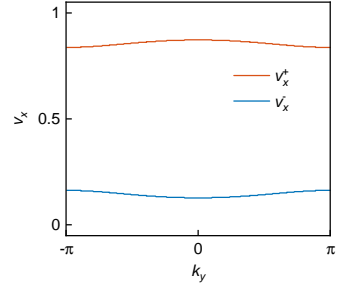


Figure C.6: The Wannier bands $v_x^\pm(k_y)$ calculated from the the Bloch Hamiltonian by means of the Wilson loop diagonalization. The circuit parameters are $C_L = 4.3 \text{ nF}$, $v_0 = 1.7$, $M = 0.3$, $J = 2$, $L_g = 1 \mu\text{H}$, $L_1 = 150 \mu\text{H}$, and $L_2 = 15 \mu\text{H}$, with the values of the other circuit elements determined accordingly.

which is indeed the case. In the k -space, the time-reversal symmetry demands that

$$TH(\mathbf{k})T^{-1} = H(-\mathbf{k}), \quad (C.13)$$

which simplifies to $H^*(\mathbf{k}) = H(-\mathbf{k})$. This condition is satisfied by Hamiltonian (C.9). Third, the model maintains the charge-conjugation symmetry, with $C = \Gamma_0 K$ acting as the charge-conjugation operator. In the k -space, this symmetry requires that

$$CH(\mathbf{k})C^{-1} = -H(-\mathbf{k}), \quad (C.14)$$

where $C = C^{-1} = \Gamma_0 K$. This condition is also satisfied by Hamiltonian (C.9). Fourth, the model preserves the C_4 symmetry up to a gauge transformation. In the k -space, this symmetry requires that

$$r_4 H(\mathbf{k}) r_4^\dagger = H(R_4 \mathbf{k}), \quad (C.15)$$

with

$$r_4 = \frac{\tau_1 + i\tau_2}{2} \otimes \sigma_0 - \frac{\tau_1 - i\tau_2}{2} \otimes i\sigma_2, \quad (C.16)$$

and R_4 representing the rotation of the momentum by $\pi/2$. This symmetry is clearly satisfied, as

$$r_4 H(k_x, k_y) r_4^\dagger = H(k_y, -k_x). \quad (C.17)$$

Fifth, considering that the chiral symmetry is defined by operator $C = \tau_3 \sigma_0$, and taking into regard that the terms representing the onsite energies in the linear lattice can be eliminated by a gauge transformation, the model also maintains the chiral symmetry, with the Hamiltonian satisfying relation

$$CH(\mathbf{k})C^\dagger = -H(\mathbf{k}). \quad (C.18)$$

Finally, the model exhibits the inversion symmetry. As the inversion symmetry I is related to the mirror symmetries by $I = m_y m_x$, the present model is indeed an inversion-symmetric one.

Due to the presence of these symmetries, the quadrupole moment q_{xy} is effectively quantized and can be calculated using the method of nested Wilson loops [3]. We first calculate the Wilson loop in the x direction, denoted as $W_{x,k}$, where $k = (k_x, k_y)$

represents the starting point of the loop. For simplicity, we denote the Bloch functions at k as $|u_k^n\rangle$, where $n = 1$ or 2 indicates the band index for the two bands below the bandgap. The components of the Bloch functions are denoted as $[u_k^n]^\alpha$ with $\alpha = 1, \dots, 4$. We define $[F_{x,k}]^{mn} = \langle u_{k+\Delta k_x}^m | u_k^n \rangle$, where $\Delta k_x = \left(\frac{2\pi}{N_x}, 0\right)$ and N_x is the number of lattice sites along the x direction. Therefore, we have

$$\mathcal{W}_{x,k} = F_{x,k+(N_x-1)\Delta k_x} \cdots F_{x,k+\Delta k_x} F_{x,k}. \quad (\text{C.19})$$

Based on the Wilson loop operator $\mathcal{W}_{x,k}$, a Wannier Hamiltonian $H_{\mathcal{W}_{x(k)}}$ can be defined via

$$\mathcal{W}_{x,k} = e^{iH_{\mathcal{W}_{x(k)}}}. \quad (\text{C.20})$$

Considering that $H_{\mathcal{W}_{x(k)}}$ has eigenvalues $2\pi v_x^j(k_y)$ for $j = +, -$, where $v_x^j(k_y)$ are the Wannier centers in the x direction, the Wilson loop can be diagonalized under fully periodic boundary conditions as

$$\mathcal{W}_{x,k} = \sum_{j=\pm} |v_{x,k}^j\rangle e^{2\pi i v_x^j(k_y)} \langle v_{x,k}^j|. \quad (\text{C.21})$$

Here, the eigenstates $|v_{x,k}^j\rangle$ for $j = +, -$ have components $[v_{x,k}^j]^n$ with $n = 1, 2$. Due to the $x \rightarrow -x$ reflection symmetry, we have $v_x^-(k_y) = -v_x^+(k_y) \bmod 1$. For the definiteness' sake, we choose $v_x^-(k_y) \in [0, 0.5]$. We set the circuit parameters as $C_L = 4.3$ nF, $v_0 = 1.7$, $M = 0.3$, $J = 2$, $L_g = 1 \mu\text{H}$, $L_1 = 150 \mu\text{H}$, and $L_2 = 15 \mu\text{H}$, with the values of the other circuit elements determined accordingly. As shown in Fig. C.6, this operation splits the original degenerate bands into two gapped Wannier sectors, labeled as v_x^- and v_x^+ . Since they are gapped, each of the Wannier sectors carries its own set of topological invariants.

We define the Wannier band subspaces as

$$|w_{x,k}^\pm\rangle = \sum_{n=1,2} |u_k^n\rangle [v_{x,k}^\pm]^n. \quad (\text{C.22})$$

Using these new subspaces, we further define $F_{y,k}^\pm = \langle w_{x,k+\Delta k_y}^\pm | w_{x,k}^\pm \rangle$, where $\Delta k_y = \left(0, \frac{2\pi}{N_y}\right)$ and N_y is the number of lattice sites along the y direction. The nested Wilson loops along k_y in the Wannier bands v_x^\pm are given by

$$\tilde{\mathcal{W}}_{y,k_x}^\pm = F_{y,k+(N_y-1)\Delta k_y}^\pm \cdots F_{y,k+\Delta k_y}^\pm F_{y,k}^\pm. \quad (\text{C.23})$$

The associated Wannier-sector polarizations are

$$p_y^{v_x^\pm} = -\frac{i}{2\pi N_x} \sum_{k_x} \log [\tilde{\mathcal{W}}_{y,k_x}^\pm] \quad (\text{C.24})$$

$$= \begin{cases} 0, & \gamma/\lambda > 1, \\ \frac{1}{2}, & \gamma/\lambda < 1, \end{cases} \quad (\text{C.25})$$

where v_x^\pm refer to the Wannier sectors. The polarization value $\frac{1}{2}$ in the y direction indicates that the Wannier Hamiltonian of the x edge, $H_{\mathcal{W}_{x(k)}}$, represents a topological insulator when $\gamma/\lambda < 1$. Similarly, we can compute the Wannier-sector polarization $p_x^{v_y^\pm}$. Finally, the quadrupole moment q_{xy}^\pm is defined as

$$q_{xy}^\pm = 2p_x^{v_y^\pm} p_y^{v_x^\pm}. \quad (\text{C.26})$$

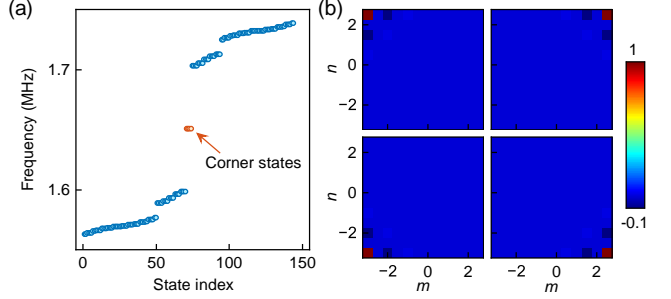


Figure C.7: **Eigenfrequencies and topological corner states of the LQTI.** (a) Eigenfrequencies of the LQTI. The four eigenfrequencies near the center (marked by red dots) correspond to the topological corner states. (b) Voltage distributions of the four topological corner states, normalized to their respective maximum values.

Due to $q_{xy}^+ \equiv q_{xy}^-$, we denote the quadrupole moment as q_{xy} . This quadrupole moment equals $\frac{1}{2}$ for $\gamma < \lambda$, and vanishes for $\gamma > \lambda$. Nonzero q_{xy} implies that the linear lattice is a topologically nontrivial one.

We next investigate a linear QTI with open boundary conditions in the x and y directions, based on the system consisting of N_x and N_y unit cells along the x and y axes, respectively. By expressing the node voltages as $V_{m,n}^{(1,2,3,4)} = \psi_{m,n}^{(1,2,3,4)} \exp(-i\bar{\omega}T)$, the governing equations can be cast in a matrix form, from which the eigenfrequencies and eigenstates of the linear QTI are obtained. We consider a circuit lattice with $N_x = N_y = 6$. The parameters of the common-cathode diodes are $C_L = 4.3$ nF, $v_0 = 1.7$, and $M = 0.3$, as determined by fitting to experimental measurements. To enhance the nonlinear response, two common-cathode diodes are used, corresponding to $J = 2$, where J is the number of diodes. The grounded inductor is fixed by setting $L_g = 1 \mu\text{H}$, and the grounded capacitor is absent, $C_g = 0$. For the system to exhibit the topological quadrupole behavior, the intracell hopping must be weaker than its intercell counterpart, i.e., $C_1 < C_2$ and $L_1 > L_2$. To satisfy the slowly-varying-envelope approximation and ensure strong localization of the corner states, the coupling inductors are chosen with $L_1 = 150 \mu\text{H}$ and $L_2 = 15 \mu\text{H}$. Based on these values, the remaining circuit elements can be determined accordingly. Figure C.7(a) presents the eigenfrequency spectrum of the linear QTI, with the four eigenfrequencies near the center (marked by red dots) corresponding to the topological corner states. Generally speaking, in the linear QTI consisting of $N_x \times N_y$ unit cells, there are four corner states, $2(N_x - 2) + 2(N_y - 2)$ edge states, and $4(N_x - 1)(N_y - 1)$ bulk states. The voltage distributions of the four topological corner states, normalized to their respective maximum values, are illustrated in Fig. C.7(b).

Appendix D. Nonlinear topological corner states and topologically trivial corner solitons

In this section, we first discuss the localization of nonlinear topological corner states and topologically trivial corner solitons. Next, we examine the topological properties of these two types of states. Finally, we address the dynamical stability or

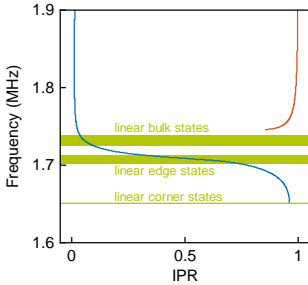


Figure D.8: **The localization of the nonlinear topological corner states and topologically trivial corner solitons.** The blue and red curves represent the IPRs of the nonlinear corner states and corner solitons, respectively.

instability of the nonlinear topological corner states and topologically trivial corner solitons.

Appendix D.1. The localization

We consider the NLQTI with open boundary conditions in the x and y directions, neglecting dissipation in the circuit lattice. By substituting $V_{m,n}^{(1,2,3,4)} = \psi_{m,n}^{(1,2,3,4)} \exp(-i\bar{\omega}T)$ into Eqs. (B.18)-(B.21), the resulting equations are solved using the Newton's method. For each value of $\bar{\omega}$, we adopted initial guesses for the voltage distributions. Once the solution is obtained at a given $\bar{\omega}$, solutions at other frequencies are derived iteratively. When searching for the nonlinear corner states, we focused on those residing in the upper-right corner of the lattice, as the four linear topological corner states (denoted by the red dots in Fig. C.7(a)) are equivalent to one another.

After obtaining the frequency spectra, we characterized the state localization by their IPR, as per Eq. (4) in the main text. When the state is strongly localized at a single lattice site, we have $\text{IPR} = 1$, whereas for a state that is uniformly distributed across the entire lattice, $\text{IPR} = (4N_x N_y)^{-1}$. Figure D.8 shows the IPRs of the nonlinear topological corner states and topologically trivial corner solitons. We first focus on the nonlinear corner states, which bifurcate from the linear corner mode. When the frequency is below that of the linear edge states, the nonlinear corner states are mainly localized at the corner site. As the frequency increases, the localization weakens. Upon entering the edge-mode band, the nonlinear corner states delocalize and, accordingly, the IPR rapidly decreases, due to the hybridization between the corner and edge states. The further increase of the frequency makes the nonlinear corner state even more delocalized, due to the hybridization with the bulk modes.

Next, we turn to the corner solitons. Being, matter-of-factly, conventional topologically trivial solitons, they become more localized with the increase of the frequency. In the strongly nonlinear regime, these solitons are strongly localized at the corner site, resulting in $\text{IPR} = 1$.

Appendix D.2. Topological properties

As discussed in Appendix C, the linear QTI satisfies several symmetry operations and the quadrupole moment q_{xy} is quantized under these symmetries. In the nonlinear case, we con-

sider three regimes: the weakly nonlinear regime, the moderately nonlinear regime, and the strongly nonlinear regime. The weakly nonlinear regime is defined as the region where nonlinear corner states are spatially localized. The moderately nonlinear regime is defined as the region where nonlinear corner states are delocalized and topologically trivial corner solitons do not exist. The strongly nonlinear regime is defined as the region where corner solitons exist. We explore the topological properties of the NLQTI in what follows below.

The onsite energy at a given lattice site of the NLQTI depends on the voltage applied to that site. Strictly speaking, inhomogeneous voltage distributions result in different onsite energies at various lattice sites, leading to the absence of discrete translational symmetry in the circuit lattice. However, in the weakly nonlinear regime, the nonlinear corner states exhibit sublattice polarization [80], allowing the NLQTI to be approximated as a linear QTI where the condition $\delta_1 = \delta_2 = \delta_3 = \delta_4$ does not hold. Specifically, the nonlinear corner state located in the upper-right corner of the lattice is polarized in sublattice 1, where the voltage is primarily distributed. This polarization allows us to construct a linear QTI as follows:

$$i \frac{dV_{m,n}^{(1)}}{dT} = [\delta_1 + g(V_{2,2}^{(1)})] V_{m,n}^{(1)} + \gamma_C V_{m,n}^{(3)} + \lambda_C V_{m+1,n}^{(3)} + \gamma_C V_{m,n}^{(4)} + \lambda_C V_{m,n+1}^{(4)}, \quad (\text{D.1})$$

$$i \frac{dV_{m,n}^{(2)}}{dT} = \delta_2 V_{m,n}^{(2)} - \gamma_L V_{m,n}^{(3)} - \lambda_L V_{m,n-1}^{(3)} + \gamma_C V_{m,n}^{(4)} + \lambda_C V_{m-1,n}^{(4)}, \quad (\text{D.2})$$

$$i \frac{dV_{m,n}^{(3)}}{dT} = \delta_3 V_{m,n}^{(3)} - \gamma_L V_{m,n}^{(2)} - \lambda_L V_{m,n+1}^{(2)} + \gamma_C V_{m,n}^{(1)} + \lambda_C V_{m-1,n}^{(1)}, \quad (\text{D.3})$$

$$i \frac{dV_{m,n}^{(4)}}{dT} = \delta_4 V_{m,n}^{(4)} + \gamma_C V_{m,n}^{(1)} + \lambda_C V_{m,n-1}^{(1)} + \gamma_C V_{m,n}^{(2)} + \lambda_C V_{m+1,n}^{(2)}, \quad (\text{D.4})$$

where $V_{2,2}^{(1)}$ represents the voltage at site 1 of the (2, 2)-th unit cell, i.e., the corner site of the circuit lattice. To verify the validity of this approximation, we calculate the eigenfrequency of the corner state in the linear QTI governed by Eqs. (D.1)-(D.4) and compare it with the eigenfrequency of the nonlinear corner state. As shown in Fig. D.9(a), the difference between the eigenfrequencies is nearly zero for the localized nonlinear corner states. In contrast, when the nonlinear corner states become delocalized, the frequency difference is significant, indicating that the approximation is no longer applicable.

In Eqs. (D.1)-(D.4), by considering the condition $\delta_1 = \delta_2 = \delta_3 = \delta_4 \equiv \delta$, we have $\delta_1 + g(V_{2,2}^{(1)}) > \delta$. As a result of these relations, both reflection symmetries m_x and m_y are broken. Furthermore, the charge-conjugation symmetry, C_4 symmetry, chiral symmetry, and inversion symmetry are all violated, only the time-reversal symmetry being preserved. We then employ the method of nested Wilson loops to calculate the quadrupole moments q_{xy}^\pm . As an example, we determine the value of $g(V_{2,2}^{(1)})$ by selecting the nonlinear corner state at a frequency of 1.67 MHz. This value is subsequently used to compute the Wannier centers

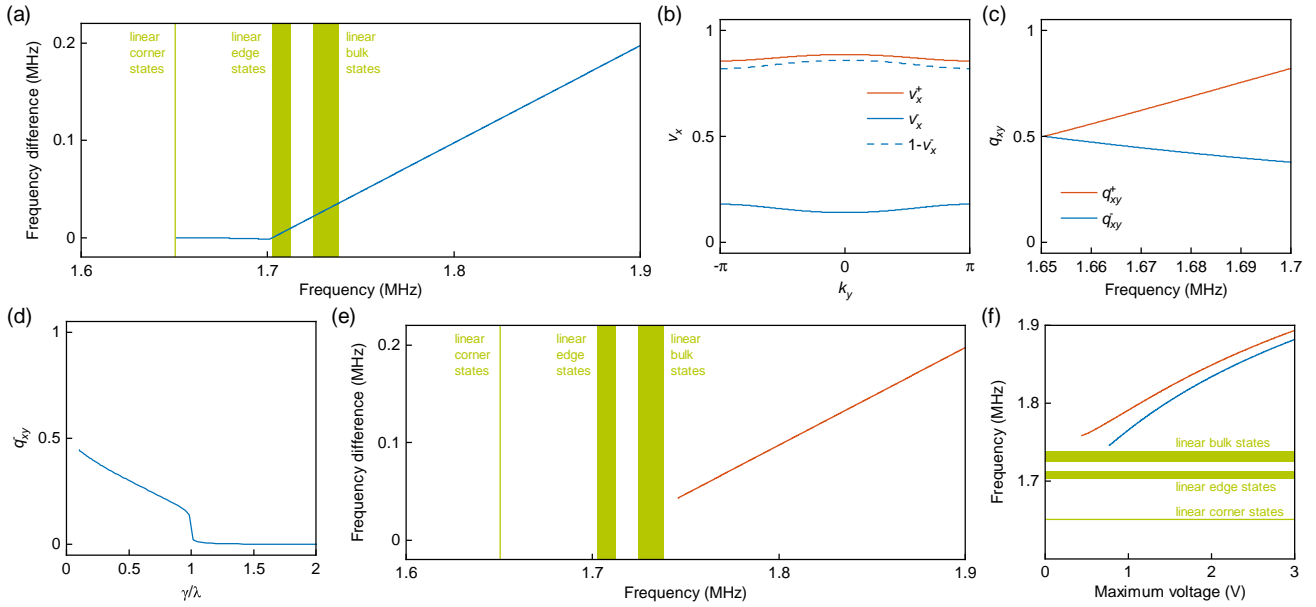


Figure D.9: Topological properties of the NLQTI. (a) The difference between the eigenfrequencies of the nonlinear corner states and those of the linear QTI, produced by Eqs. (D.1)-(D.4). (b) The Wannier bands $v_x^\pm(k_y)$ calculated from the Bloch Hamiltonian derived from Eqs. (D.1)-(D.4). For comparison, $1 - v_x^-(k_y)$ is also plotted as a dashed curve. The value of $g(V_{2,2}^{(1)})$ is determined by selecting the nonlinear corner state at the frequency of 1.67 MHz. (c) The quadrupole moments q_{xy}^\pm , labeled with \pm for their respective Wannier sectors, at various frequencies of the nonlinear topological corner states. (d) The dependence of the quadrupole moment q_{xy}^- on the dimerization ratio γ/λ . The value of $g(V_{2,2}^{(1)})$, obtained by selecting the nonlinear corner state at a frequency of 1.67 MHz, is used for calculations at different dimerization ratios. (e) The difference between the eigenfrequencies of the corner solitons and those of the LQTI governed by Eqs. (D.1)-(D.4). (f) The dependence of the eigenfrequency of the corner solitons on the maximum voltage in the lattice. The red and blue curves represent the corner solitons calculated from Eqs. (B.18)-(B.21) and Eqs. (D.5)-(D.8), respectively.

by following the procedure outlined in Appendix C. We find that the two Wannier sectors, v_x^- and v_x^+ , remain gapped; however, $v_x^-(k_y) \neq -v_x^+(k_y) \bmod 1$ due to the violation of reflection symmetry in the x direction, as demonstrated in Fig. D.9(b). For comparison, we also plot $1 - v_x^-(k_y)$ as a dashed curve.

In the linear QTI phase, the Wannier sector polarizations p_x^{\pm} are quantized due to the presence of two anti-commuting reflection symmetries m_x and m_y . However, in the nonlinear case, these reflection symmetries are violated, resulting in p_x^{\pm} not being quantized. Similarly, we find that the Wannier sector polarizations p_y^{\pm} are also not quantized. Consequently, the quadrupole moments q_{xy}^\pm , labeled with \pm to denote the respective Wannier sectors, do not equal the quantized value of $1/2$, as shown in Fig. D.9(c). Note that $q_{xy}^+ \neq q_{xy}^- \neq 1/2$ when the frequency deviates from that of the linear topological corner state.

Furthermore, when we evaluate the dependence of the quadrupole moment q_{xy}^- on the dimerization ratio γ/λ , we observe that q_{xy}^- varies continuously, as illustrated in Fig. D.9(d). However, the quadrupole moment remains strictly positive when $\gamma < \lambda$, in contrast to the nearly zero values observed when $\gamma > \lambda$. In our calculations, we use the same value of $g(V_{2,2}^{(1)})$ for different dimerization ratios. Specifically, this value is determined by selecting the nonlinear corner state at a frequency of 1.67 MHz. Therefore, these results imply that in this weakly nonlinear regime, the nonzero quadrupole invariant can still be used to demonstrate that the corner states are topologically non-

trivial ones, exhibiting robustness against perturbations induced by onsite nonlinearity.

In the moderately nonlinear regime, as shown in Fig. D.9(a), the approximations for the onsite energies are no longer valid, and Eqs. (D.1)-(D.4) are no longer applicable for characterizing the topological properties of the NLQTI. The delocalized field distribution leads to a breakdown of the periodicity in the circuit lattice. Consequently, the definition of the quadrupole moments q_{xy}^\pm , introduced in Appendix C, cannot be applied in this context. In fact, due to the competition between onsite perturbations and intersite hoppings, localized states are absent in this moderately nonlinear regime.

In the regime of strong nonlinearity, the approximations for the onsite energies become invalid. As shown in Fig. D.9(e), the difference between the eigenfrequencies of the corner solitons and those of the linear QTI governed by Eqs. (D.1)-(D.4) is significant, indicating that these equations are not suitable for characterizing the topological properties of the NLQTI. Instead, we will approach the topological property of the NLQTI in the strongly nonlinear regime from a different perspective.

From Eqs. (B.18)-(B.21), as the onsite energies dominate the difference between the intracell and intercell hopping strengths,

we can approximate Eqs. (B.18)-(B.21) as follows:

$$\begin{aligned} i \frac{dV_{m,n}^{(1)}}{dT} &= \delta_1 V_{m,n}^{(1)} + \chi_C V_{m,n}^{(3)} + \chi_C V_{m+1,n}^{(3)} + \chi_C V_{m,n}^{(4)} + \chi_C V_{m,n+1}^{(4)} \\ &+ g(V_{m,n}^{(1)}) V_{m,n}^{(1)}, \end{aligned} \quad (\text{D.5})$$

$$\begin{aligned} i \frac{dV_{m,n}^{(2)}}{dT} &= \delta_2 V_{m,n}^{(2)} - \chi_L V_{m,n}^{(3)} - \chi_L V_{m,n-1}^{(3)} + \chi_C V_{m,n}^{(4)} + \chi_C V_{m-1,n}^{(4)} \\ &+ g(V_{m,n}^{(2)}) V_{m,n}^{(2)}, \end{aligned} \quad (\text{D.6})$$

$$\begin{aligned} i \frac{dV_{m,n}^{(3)}}{dT} &= \delta_3 V_{m,n}^{(3)} - \chi_L V_{m,n}^{(2)} - \chi_L V_{m,n+1}^{(2)} + \chi_C V_{m,n}^{(1)} + \chi_C V_{m-1,n}^{(1)} \\ &+ g(V_{m,n}^{(3)}) V_{m,n}^{(3)}, \end{aligned} \quad (\text{D.7})$$

$$\begin{aligned} i \frac{dV_{m,n}^{(4)}}{dT} &= \delta_4 V_{m,n}^{(4)} + \chi_C V_{m,n}^{(1)} + \chi_C V_{m,n-1}^{(1)} + \chi_C V_{m,n}^{(2)} + \chi_C V_{m+1,n}^{(2)} \\ &+ g(V_{m,n}^{(4)}) V_{m,n}^{(4)}, \end{aligned} \quad (\text{D.8})$$

where $\chi_C = (\gamma_C + \lambda_C)/2$ and $\chi_L = (\gamma_L + \lambda_L)/2$. Since $\chi_C = \chi_L$ under our circuit parameters, these equations describe a nonlinear lattice with equal intracell and intercell hopping strengths, resulting in no dimerization. In the linear case with $g = 0$, this lattice is gapless and does not support topological corner states. However, under the action of the nonlinearity, this lattice can support conventional self-trapped states, commonly referred to as surface solitons [76, 77, 78]. In our study, we denote these self-trapped states as corner solitons because they are localized at the lattice corners. In Fig. D.9(f), we illustrate the dependence of the eigenfrequency of the corner soliton on the maximum voltage in the lattice, calculated using Eqs. (D.5)-(D.8), represented by the red curve. For comparison, we include the curve for the corner soliton obtained from Eqs. (B.18)-(B.21), indicated by the blue curve. The corner solitons from both types of lattice models exist within the semi-infinite gap, indicating that they share the same physical origin: their existence is entirely induced by nonlinearity, rendering them topologically trivial.

When the maximum voltage becomes sufficiently large, that is, in the ultra-strongly nonlinear regime, the hopping strengths χ_C and χ_L can be neglected compared to the onsite energies [67]. In this case, Eqs. (D.5)-(D.8) further reduce to

$$i \frac{dV_{2,2}^{(1)}}{dT} = \delta_1 V_{2,2}^{(1)} + g(V_{2,2}^{(1)}) V_{2,2}^{(1)}, \quad (\text{D.9})$$

which governs a nonlinear single lattice site. Solving this equation reveals that the corner soliton is localized at a single corner site.

Appendix D.3. The stability analysis

The stability of nonlinear states is their crucially important property, as only stable states can be excited and observed experimentally. We investigated the dynamical stability of the nonlinear topological corner states and topologically trivial corner solitons by means of the standard linear-stability analysis. To this end, perturbed solutions

$$V_{m,n}^{(j)} = e^{-i\bar{\omega}T} \left(\psi_{m,n}^{(j)} + \varepsilon_{m,n}^{(j)} e^{-i\zeta T} + \mu_{m,n}^{(j)*} e^{i\zeta^* T} \right), \quad (\text{D.10})$$

with $j = 1, 2, 3, 4$, were substituted into Eqs. (B.18)-(B.21). Here $\psi_{m,n}^{(j)}$ is the unperturbed solution representing the nonlinear corner states or corner solitons, $\varepsilon_{m,n}^{(j)}$ and $\mu_{m,n}^{(j)}$ are infinitesimal amplitudes of the perturbations, which correspond to eigenvalue ζ , and $\bar{\omega}$ is the normalized eigenfrequency defined as $\bar{\omega} = \omega/\omega_n$. The nonlinear corner states or corner solitons are linearly stable if the imaginary part of ζ (i.e., the growth rate) is positive. The linearization leads to the following equations:

$$\begin{aligned} -\bar{\omega} \varepsilon_{m,n}^{(1)} + \delta_1 \varepsilon_{m,n}^{(1)} + \gamma_C \varepsilon_{m,n}^{(3)} + \gamma_C \varepsilon_{m,n}^{(4)} + \lambda_C \varepsilon_{m+1,n}^{(3)} + \lambda_C \varepsilon_{m,n+1}^{(4)} \\ + g(\psi_{m,n}^{(1)}) \varepsilon_{m,n}^{(1)} + g_1(\psi_{m,n}^{(1)}) \psi_{m,n}^{(1)*} \mu_{m,n}^{(1)} + g_1(\psi_{m,n}^{(1)}) |\psi_{m,n}^{(1)}|^2 \varepsilon_{m,n}^{(1)} \end{aligned} \quad (\text{D.11})$$

$$\begin{aligned} = \zeta \varepsilon_{m,n}^{(1)}, \\ \bar{\omega} \mu_{m,n}^{(1)} - \delta_1 \mu_{m,n}^{(1)} - \gamma_C \mu_{m,n}^{(3)} - \gamma_C \mu_{m,n}^{(4)} - \lambda_C \mu_{m+1,n}^{(3)} - \lambda_C \mu_{m,n+1}^{(4)} \\ - g(\psi_{m,n}^{(1)}) \mu_{m,n}^{(1)} - g_1(\psi_{m,n}^{(1)}) \psi_{m,n}^{(1)*} \varepsilon_{m,n}^{(1)} - g_1(\psi_{m,n}^{(1)}) |\psi_{m,n}^{(1)}|^2 \mu_{m,n}^{(1)} \end{aligned} \quad (\text{D.12})$$

$$\begin{aligned} = \zeta \mu_{m,n}^{(1)}, \\ -\bar{\omega} \varepsilon_{m,n}^{(2)} + \delta_2 \varepsilon_{m,n}^{(2)} + \gamma_C \varepsilon_{m,n}^{(4)} - \gamma_L \varepsilon_{m,n}^{(3)} + \lambda_C \varepsilon_{m-1,n}^{(4)} - \lambda_L \varepsilon_{m,n-1}^{(3)} \\ + g(\psi_{m,n}^{(2)}) \varepsilon_{m,n}^{(2)} + g_1(\psi_{m,n}^{(2)}) \psi_{m,n}^{(2)*} \mu_{m,n}^{(2)} + g_1(\psi_{m,n}^{(2)}) |\psi_{m,n}^{(2)}|^2 \varepsilon_{m,n}^{(2)} \end{aligned} \quad (\text{D.13})$$

$$\begin{aligned} = \zeta \varepsilon_{m,n}^{(2)}, \\ \bar{\omega} \mu_{m,n}^{(2)} - \delta_2 \mu_{m,n}^{(2)} - \gamma_C \mu_{m,n}^{(4)} + \gamma_L \mu_{m,n}^{(3)} - \lambda_C \mu_{m-1,n}^{(4)} + \lambda_L \mu_{m,n-1}^{(3)} \\ - g(\psi_{m,n}^{(2)}) \mu_{m,n}^{(2)} - g_1(\psi_{m,n}^{(2)}) \psi_{m,n}^{(2)*} \varepsilon_{m,n}^{(2)} - g_1(\psi_{m,n}^{(2)}) |\psi_{m,n}^{(2)}|^2 \mu_{m,n}^{(2)} \end{aligned} \quad (\text{D.14})$$

$$\begin{aligned} = \zeta \mu_{m,n}^{(2)}, \\ -\bar{\omega} \varepsilon_{m,n}^{(3)} + \delta_3 \varepsilon_{m,n}^{(3)} + \gamma_C \varepsilon_{m,n}^{(1)} - \gamma_L \varepsilon_{m,n}^{(2)} + \lambda_C \varepsilon_{m-1,n}^{(1)} - \lambda_L \varepsilon_{m,n-1}^{(2)} \\ + g(\psi_{m,n}^{(3)}) \varepsilon_{m,n}^{(3)} + g_1(\psi_{m,n}^{(3)}) \psi_{m,n}^{(3)*} \mu_{m,n}^{(3)} + g_1(\psi_{m,n}^{(3)}) |\psi_{m,n}^{(3)}|^2 \varepsilon_{m,n}^{(3)} \end{aligned} \quad (\text{D.15})$$

$$\begin{aligned} = \zeta \varepsilon_{m,n}^{(3)}, \\ \bar{\omega} \mu_{m,n}^{(3)} - \delta_3 \mu_{m,n}^{(3)} - \gamma_C \mu_{m,n}^{(1)} + \gamma_L \mu_{m,n}^{(2)} - \lambda_C \mu_{m-1,n}^{(1)} + \lambda_L \mu_{m,n+1}^{(2)} \\ - g(\psi_{m,n}^{(3)}) \mu_{m,n}^{(3)} - g_1(\psi_{m,n}^{(3)}) \psi_{m,n}^{(3)*} \varepsilon_{m,n}^{(3)} - g_1(\psi_{m,n}^{(3)}) |\psi_{m,n}^{(3)}|^2 \mu_{m,n}^{(3)} \end{aligned} \quad (\text{D.16})$$

$$\begin{aligned} = \zeta \mu_{m,n}^{(3)}, \\ -\bar{\omega} \varepsilon_{m,n}^{(4)} + \delta_4 \varepsilon_{m,n}^{(4)} + \gamma_C \varepsilon_{m,n}^{(2)} + \gamma_C \varepsilon_{m,n}^{(1)} + \lambda_C \varepsilon_{m+1,n}^{(2)} + \lambda_C \varepsilon_{m,n-1}^{(1)} \\ + g(\psi_{m,n}^{(4)}) \varepsilon_{m,n}^{(4)} + g_1(\psi_{m,n}^{(4)}) \psi_{m,n}^{(4)*} \mu_{m,n}^{(4)} + g_1(\psi_{m,n}^{(4)}) |\psi_{m,n}^{(4)}|^2 \varepsilon_{m,n}^{(4)} \end{aligned} \quad (\text{D.17})$$

$$\begin{aligned} = \zeta \mu_{m,n}^{(4)}, \\ \bar{\omega} \mu_{m,n}^{(4)} - \delta_4 \mu_{m,n}^{(4)} - \gamma_C \mu_{m,n}^{(2)} - \gamma_C \mu_{m,n}^{(1)} - \lambda_C \mu_{m+1,n}^{(2)} - \lambda_C \mu_{m,n-1}^{(1)} \\ - g(\psi_{m,n}^{(4)}) \mu_{m,n}^{(4)} - g_1(\psi_{m,n}^{(4)}) \psi_{m,n}^{(4)*} \varepsilon_{m,n}^{(4)} - g_1(\psi_{m,n}^{(4)}) |\psi_{m,n}^{(4)}|^2 \mu_{m,n}^{(4)} \end{aligned} \quad (\text{D.18})$$

where

$$g_1(\psi_{m,n}^{(j)}) = \frac{J}{4(C_g + J C_L)} \left[\frac{MC_L}{\left(1 + |\psi_{m,n}^{(j)}/v_0| \right)^{M+1}} \frac{1}{v_0 |\psi_{m,n}^{(j)}|} \right] \frac{\omega_0}{\omega_n} \quad (\text{D.19})$$

with $j = 1, 2, 3, 4$.

To confirm the expected stability or instability of the nonlinear corner states and corner solitons, we simulated their temporal evolution in the framework of full equations (B.18)-(B.21). For this purpose, we used the Runge-Kutta algorithm, adding initial random perturbations at the level of $\pm 2\%$ to the eigenstates and evaluating ratio P_1/P during the evolution, where

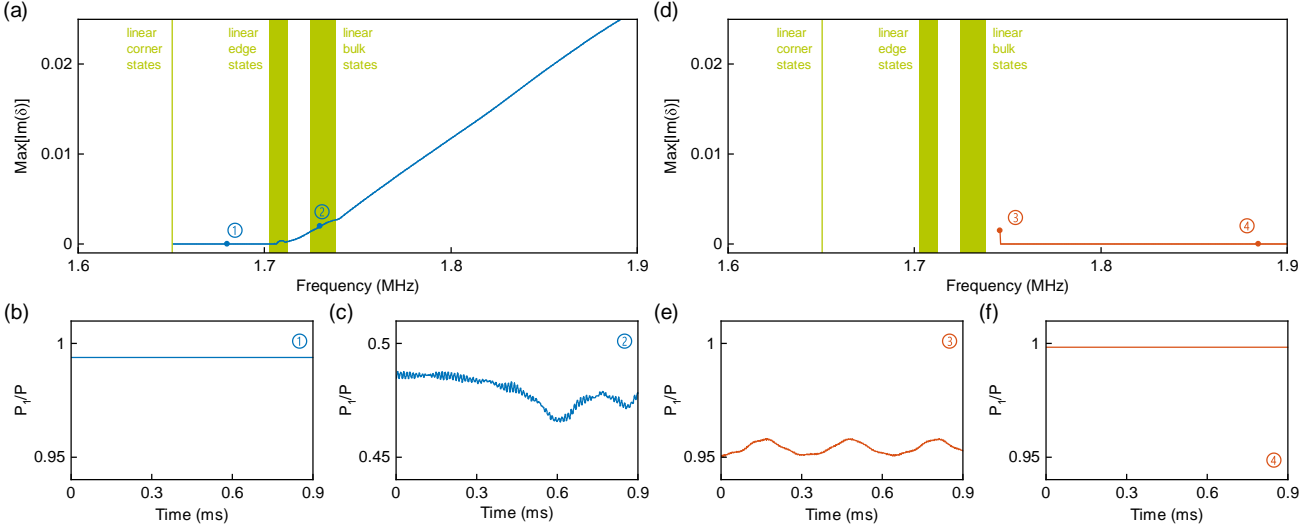


Figure D.10: **The stability analysis for the nonlinear topological corner states and topologically trivial corner solitons.** (a) The maximum perturbation growth rates, $\text{Max}[\text{Im}(\delta)]$, of the nonlinear corner states. (b)-(c) The evolution of the eigenstates labeled in (a), with noise at the $\pm 2\%$ level added to the input. The ratio P_1/P quantifies the fraction of the total power carried by the sublattice of sites 1 across the entire system. (d) The maximum growth rates, $\text{Max}[\text{Im}(\delta)]$, of the corner solitons. (e)-(f) The evolution of the eigenstates labeled in (d), with the $\pm 2\%$ noise added to the input.

$P_j = \sum_{m,n} \left| \psi_{m,n}^{(j)} \right|^2$ ($j = 1, 2, 3, 4$) and $P = \sum_{j=1}^4 P_j$. This ratio quantifies the fraction of the power carried by the sublattice j across the entire lattice. A sufficiently small time-matching step is chosen to ensure the accuracy of the simulation results.

Figures D.10(a)-(c) illustrate the stability of the nonlinear topological corner states. In panel (a), we observe that the maximum perturbation growth rate, $\text{Max}[\text{Im}(\delta)]$, remains zero until the frequency enters the band associated with the linear edge states. This indicates that the nonlinear corner states are linearly stable when they are well localized at the lattice corner. When the frequency enters the edge band, $\text{Max}[\text{Im}(\delta)]$ gradually increases following the increase of the frequency, leading to the linear instability of the delocalized nonlinear corner states. The simulation results produced by the direct simulations of the evolution confirm the predictions made by the linear stability analysis. As shown in Fig. D.10(b), for state ①, which is a linearly stable one, ratio P_1/P remains constant during the evolution. On the other hand, state ②, which belongs to the linearly unstable regime, P_1/P exhibits significant variance, as seen in Fig. D.10(c).

Figures D.10(d)-(f) display results of the stability analysis for the topologically trivial corner solitons. In panel (d), the maximum perturbation growth rate, $\text{Max}[\text{Im}(\delta)]$, is nonzero only at the smallest frequency. At all other frequencies, $\text{Max}[\text{Im}(\delta)] = 0$, which implies that the corner solitons are linearly unstable at the smallest frequency, and stable at all other frequencies. This conclusion is confirmed by the simulations of the perturbed evolution. As shown in Fig. D.10(e), for state ③, which corresponds to the smallest frequency, ratio P_1/P slightly oscillates during the evolution, demonstrating its weak instability. In contrast, for state ④, which belongs to the linearly stable regime, P_1/P remains constant, as seen in Fig. D.10(f).

Appendix E. Bulk solitons

We investigated the solitons that reside in the bulk of the NLQTI. We employed the anti-continuum limit to identify the initial solutions, which were then used to produce the bulk soliton solutions. Subsequently, we conducted the stability analysis for various types of bulk solitons. Note that for a NLQTI, governed by Eqs. (B.18)-(B.21), the parameters satisfy the constraints $\delta_1 = \delta_2 = \delta_3 = \delta_4 \equiv \delta$, $\lambda_C = \lambda_L \equiv \lambda$, and $\gamma_C = \gamma_L \equiv \gamma$.

Appendix E.1. Soliton solutions in the anti-continuum limit

First, we set the intercell hopping to be $\lambda = 0$, which simplifies the governing equations to:

$$[\bar{\omega} - \delta - g(\psi_{m,n}^{(1)})] \psi_{m,n}^{(1)} = \gamma \psi_{m,n}^{(3)} + \gamma \psi_{m,n}^{(4)}, \quad (\text{E.1})$$

$$[\bar{\omega} - \delta - g(\psi_{m,n}^{(2)})] \psi_{m,n}^{(2)} = \gamma \psi_{m,n}^{(4)} - \gamma \psi_{m,n}^{(3)}, \quad (\text{E.2})$$

$$[\bar{\omega} - \delta - g(\psi_{m,n}^{(3)})] \psi_{m,n}^{(3)} = \gamma \psi_{m,n}^{(1)} - \gamma \psi_{m,n}^{(2)}, \quad (\text{E.3})$$

$$[\bar{\omega} - \delta - g(\psi_{m,n}^{(4)})] \psi_{m,n}^{(4)} = \gamma \psi_{m,n}^{(2)} + \gamma \psi_{m,n}^{(1)}. \quad (\text{E.4})$$

Solving these equations in the general form is quite challenging. Here, we only consider four special cases.

(1) We assume that $\psi_{m,n}^{(2)} = 0$ and $\psi_{m,n}^{(3)} = \psi_{m,n}^{(4)}$. Under these conditions, the four equations reduce to two:

$$[\bar{\omega} - \delta - g(\psi_{m,n}^{(1)})] \psi_{m,n}^{(1)} = 2\gamma \psi_{m,n}^{(3)}, \quad (\text{E.5})$$

$$[\bar{\omega} - \delta - g(\psi_{m,n}^{(3)})] \psi_{m,n}^{(3)} = \gamma \psi_{m,n}^{(1)}. \quad (\text{E.6})$$

We also assume that the solutions are real. These equations can then be solved numerically, usually supporting three types of soliton solutions. For the sake of simplicity in comparison, we refer to these soliton solutions as quasi-symmetric solitons, quasi-antisymmetric solitons, and asymmetric solitons.

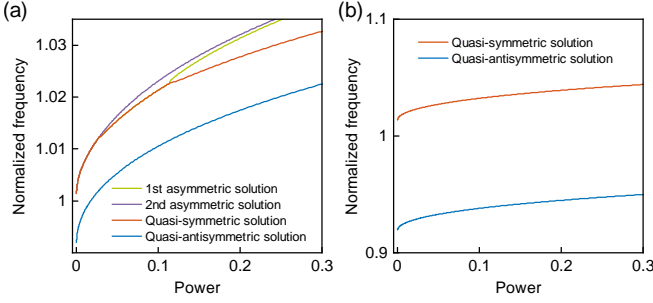


Figure E.11: Soliton families obtained in the anti-continuum limit. (a) The solutions obtained in the limit of $\lambda = 0$. (b) The solutions obtained in the limit of $\gamma = 0$.

(2) We assume that $\psi_{m,n}^{(4)} = 0$ and $\psi_{m,n}^{(1)} = -\psi_{m,n}^{(2)}$. Under these assumptions, the four equations reduce to the following pair:

$$[\bar{\omega} - \delta - g(\psi_{m,n}^{(1)})] \psi_{m,n}^{(1)} = \gamma \psi_{m,n}^{(3)}, \quad (E.7)$$

$$[\bar{\omega} - \delta - g(\psi_{m,n}^{(3)})] \psi_{m,n}^{(3)} = 2\gamma \psi_{m,n}^{(1)}. \quad (E.8)$$

These equations can be obtained from those in case (1) by a transformation: $\psi_{m,n}^{(1)} \rightarrow \psi_{m,n}^{(3)}$, $\psi_{m,n}^{(3)} \rightarrow \psi_{m,n}^{(1)}$, $\psi_{m,n}^{(2)} \rightarrow -\psi_{m,n}^{(4)}$, and $\psi_{m,n}^{(4)} \rightarrow -\psi_{m,n}^{(2)}$. The solitons derived from this case are tantamount to those in case (1) due to reflection symmetry m_x .

(3) We set $\psi_{m,n}^{(3)} = 0$ and $\psi_{m,n}^{(1)} = \psi_{m,n}^{(2)}$. Under these assumptions, the four equations reduce to the following pair:

$$[\bar{\omega} - \delta - g(\psi_{m,n}^{(2)})] \psi_{m,n}^{(2)} = \gamma \psi_{m,n}^{(4)}, \quad (E.9)$$

$$[\bar{\omega} - \delta - g(\psi_{m,n}^{(4)})] \psi_{m,n}^{(4)} = 2\gamma \psi_{m,n}^{(2)}. \quad (E.10)$$

These equations can be obtained from those in case (1) by another set of transformations: $\psi_{m,n}^{(1)} \rightarrow \psi_{m,n}^{(4)}$, $\psi_{m,n}^{(3)} \rightarrow \psi_{m,n}^{(2)}$, $\psi_{m,n}^{(4)} \rightarrow \psi_{m,n}^{(1)}$, and $\psi_{m,n}^{(2)} \rightarrow \psi_{m,n}^{(3)}$. In this case, the solitons are tantamount in case (1) due to reflection symmetry m_y .

(4) We assume that $\psi_{m,n}^{(1)} = 0$ and $\psi_{m,n}^{(3)} = -\psi_{m,n}^{(4)}$. Under these assumptions, the four equations reduce to another set of two equations:

$$[\bar{\omega} - \delta - g(\psi_{m,n}^{(2)})] \psi_{m,n}^{(2)} = 2\gamma \psi_{m,n}^{(4)}, \quad (E.11)$$

$$[\bar{\omega} - \delta - g(\psi_{m,n}^{(4)})] \psi_{m,n}^{(4)} = \gamma \psi_{m,n}^{(2)}. \quad (E.12)$$

They can be obtained from those in case (2) by an appropriate transformation, $\psi_{m,n}^{(1)} \rightarrow \psi_{m,n}^{(4)}$, $\psi_{m,n}^{(3)} \rightarrow \psi_{m,n}^{(2)}$, $\psi_{m,n}^{(4)} \rightarrow \psi_{m,n}^{(1)}$, and $\psi_{m,n}^{(2)} \rightarrow \psi_{m,n}^{(3)}$. The solitons derived from this case are tantamount to those in case (2) due to reflection symmetry m_y .

From the above discussion, one finds that the four cases are tantamount to one another, and the soliton solutions in these cases can be transformed by symmetry operations. Therefore, we now focus the study exclusively on the soliton solutions in case (1). In the context of the circuit lattice, $\lambda = 0$ implies $C_2 = 0$ and $L_2 = \infty$. In the linear limit with $g = 0$, Eqs. (E.5) and (E.6) yield only two solutions: one is $\psi_{m,n}^{(1)} = \sqrt{2}\psi_{m,n}^{(3)}$ with the normalized eigenfrequency $\bar{\omega} = \delta + \sqrt{2}\gamma$, and the other one is $\psi_{m,n}^{(1)} = -\sqrt{2}\psi_{m,n}^{(3)}$ with $\bar{\omega} = \delta - \sqrt{2}\gamma$. In the presence of the nonlinearity, i.e., when $g \neq 0$, Eqs. (E.5) and (E.6) may support additional solutions. Fig. E.11(a) presents the relationship between the soliton's power and normalized frequency $\bar{\omega}$, with the

power defined as $P = |\psi_{m,n}^{(1)}|^2 + |\psi_{m,n}^{(3)}|^2$. From the figure, we observe that Eqs. (E.5) and (E.6) support four types of soliton solutions: quasi-symmetric, quasi-antisymmetric, and two asymmetric ones. The quasi-symmetric and quasi-antisymmetric solutions (plotted by the red and blue curves, respectively) bifurcate from the linear-limit solutions, while the two asymmetric solutions (yellow-green and purple curves) both bifurcate from the quasi-symmetric one.

Second, we set the intracell hopping to be $\gamma = 0$, which reduces the governing equations to the following system:

$$[\bar{\omega} - \delta - g(\psi_{m,n}^{(1)})] \psi_{m,n}^{(1)} = \lambda \psi_{m+1,n}^{(3)} + \lambda \psi_{m,n+1}^{(4)}, \quad (E.13)$$

$$[\bar{\omega} - \delta - g(\psi_{m+1,n+1}^{(2)})] \psi_{m+1,n+1}^{(2)} = \lambda \psi_{m,n+1}^{(4)} - \lambda \psi_{m+1,n}^{(3)}, \quad (E.14)$$

$$[\bar{\omega} - \delta - g(\psi_{m+1,n}^{(3)})] \psi_{m+1,n}^{(3)} = \lambda \psi_{m,n}^{(1)} - \lambda \psi_{m+1,n+1}^{(2)}, \quad (E.15)$$

$$[\bar{\omega} - \delta - g(\psi_{m,n+1}^{(4)})] \psi_{m,n+1}^{(4)} = \lambda \psi_{m+1,n+1}^{(2)} + \lambda \psi_{m,n}^{(1)}. \quad (E.16)$$

This case too gives rise to four special solutions. Here, we focus on the case with $\psi_{m+1,n+1}^{(2)} = 0$ and $\psi_{m+1,n}^{(3)} = \psi_{m,n+1}^{(4)}$, when the four equations reduce to two:

$$[\bar{\omega} - \delta - g(\psi_{m,n}^{(1)})] \psi_{m,n}^{(1)} = 2\lambda \psi_{m+1,n}^{(3)}, \quad (E.17)$$

$$[\bar{\omega} - \delta - g(\psi_{m+1,n}^{(3)})] \psi_{m+1,n}^{(3)} = \lambda \psi_{m,n}^{(1)}. \quad (E.18)$$

In the context of the circuit lattice, $\gamma = 0$ implies $C_1 = 0$ and $L_1 = \infty$. In the linear limit with $g = 0$, Eqs. (E.17) and (E.18) yield only two solutions: one with $\psi_{m,n}^{(1)} = \sqrt{2}\psi_{m+1,n}^{(3)}$ and the normalized eigenfrequency $\bar{\omega} = \delta + \sqrt{2}\lambda$, and the other one with $\psi_{m,n}^{(1)} = -\sqrt{2}\psi_{m+1,n}^{(3)}$ and $\bar{\omega} = \delta - \sqrt{2}\lambda$. In contrast to the case of $\lambda = 0$, only two solutions exist if the nonlinearity is present: one quasi-symmetric and one quasi-antisymmetric, as shown in Fig. E.11(b). Both the quasi-symmetric and quasi-antisymmetric solutions bifurcate from the linear-limit ones.

Appendix E.2. The existence of bulk solitons

First, extending the analysis, we investigate the bulk solitons that are continuations of the solitons in the case of $\lambda = 0$. We use the soliton solutions obtained in the anti-continuum limit as the input in the Newton's method and find the soliton solutions, gradually increasing C_2 from 0 to the target value. Figure E.12(a) presents the relationship between the frequency and soliton power $P = \sum_{m,n,j} |\psi_{m,n}^{(j)}|^2$. The solid blue and red curves represent the quasi-antisymmetric and quasi-symmetric bulk solitons, respectively, while the solid yellow-green and purple curves correspond to two types of asymmetric bulk solitons. Voltage distributions in typical solitons labeled in (a) are shown in Fig. E.12(b). From Fig. E.12(a), we find that all four types of the bulk solitons reside in the semi-infinite gap. These soliton branches terminate at small powers, due to the inability of the Newton's method to capture poorly localized solutions. All these bulk solitons are conventional lattice solitons. As shown in Fig. E.13(a), they are more localized at higher power, which is equivalent to enhanced nonlinearity.

Second, we investigate the bulk solitons that are continuations of the soliton solutions found at $\gamma = 0$. As there are only two solutions in the anti-continuum limit, the bulk solitons

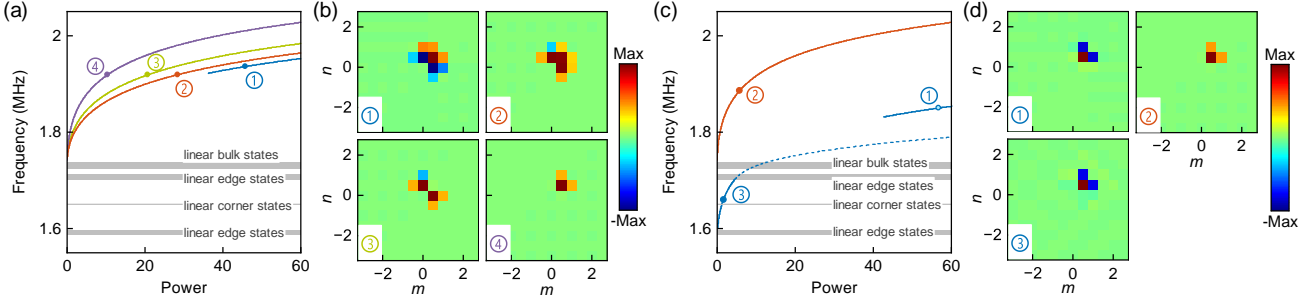


Figure E.12: Bulk solitons in the NLQTI. (a)-(b) Bulk solitons that are the continuation of the solitons found at $\lambda = 0$. Panel (a) shows the relationship between the frequency and soliton power, with panel (b) presenting voltage distributions of typical solitons labeled in (a). The solid blue and red curves represent the quasi-antisymmetric and quasi-symmetric bulk solitons, respectively, while the yellow-green and purple curves correspond to the two types of asymmetric bulk solitons. (c)-(d) Bulk solitons that are continuations of the solitons found at $\gamma = 0$. Panel (c) presents the relationship between the frequency and soliton power, (d) displaying voltage distributions of typical solitons labeled in (c). The solid blue and red curves again denote the quasi-antisymmetric and quasi-symmetric bulk solitons, respectively, while the dashed blue curve indicates the delocalized states arising from one type of the quasi-antisymmetric bulk soliton. It is worthy to note that there are two branches of quasi-antisymmetric bulk solitons: one residing in the middle finite gap between bands of the linear edge states, and the other one in the semi-infinite gap.

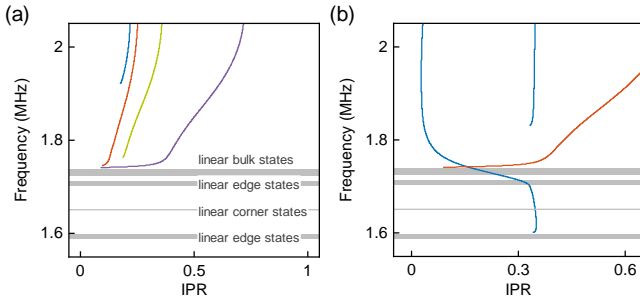


Figure E.13: IPRs of the bulk solitons in the NLQTI. (a) IPRs of the bulk solitons that are continuations of the solitons found at $\lambda = 0$. The blue and red curves represent the quasi-antisymmetric and quasi-symmetric bulk solitons, respectively, while the yellow-green and purple curves correspond to the two types of asymmetric bulk solitons. (b) IPRs of the bulk solitons that are continuations of the solitons found at $\gamma = 0$. The blue and red curves again denote the quasi-antisymmetric and quasi-symmetric bulk solitons, respectively. Note that the delocalized states arising from the quasi-antisymmetric bulk solitons are also represented in the figure.

in this case also exhibit solely quasi-antisymmetric and quasi-symmetric distributions. However, we find that there are two different branches of quasi-antisymmetric bulk solitons: one residing in the middle finite gap between bands of the linear edge states, and the other one in the semi-infinite gap, as shown in Fig. E.12(c). The solid blue and red curves again denote the quasi-antisymmetric and quasi-symmetric bulk solitons, respectively, while the dashed blue curve indicates the delocalized states arising from one type of the quasi-antisymmetric bulk soliton. The voltage distributions of typical solitons labeled in (c) are plotted in Fig. E.12(d). Figure E.13(b) displays IPRs of these bulk solitons. For the quasi-symmetric and quasi-antisymmetric ones, located in the semi-infinite gap, IPR increases with the frequency. In contrast, the quasi-antisymmetric bulk solitons residing in the middle finite gap exhibit weak localization near the upper and lower band edges of the linear edge states.

Appendix E.3. Stability/instability of the bulk solitons

We studied the stability of the bulk solitons by means of the linear-stability analysis. Figure E.14(a) shows the maximum perturbation growth rates, $\text{Max} [\text{Im}(\delta)]$, of the bulk solitons that are continuations of the ones found at $\lambda = 0$. The blue and red curves represent the quasi-antisymmetric and quasi-symmetric bulk solitons, respectively, while the yellow-green and purple curves correspond to the two types of asymmetric bulk solitons. The family of the quasi-antisymmetric solitons (denoted by the blue curve) shows linear instability at low frequencies. In view of these instabilities and the weak localization (see the blue curve in Fig. E.13(a)), the quasi-antisymmetric solitons can hardly be excited using quench dynamics. Similarly, the quasi-symmetric solitons cannot be excited either, due to the strong instability (see the red curve in Fig. E.14(a)) and weak localization (the red curve in Fig. E.13(a)). The first type of the asymmetric bulk solitons (denoted by the yellow-green curve in Fig. E.14(a)), shows linear instability too, which again denies the possibility to observe them in the experiment. The asymmetric bulk solitons of the second type are linearly stable (see the purple curve in Fig. E.14(a)), their localization is weak in the case of weak nonlinearity (see the purple curve in Fig. E.13(a)). While the asymmetric bulk solitons of the second type are strongly localized under the action of strong nonlinearity, the IPR shows that their structure (voltage distribution) deviates from the initial three-site excitation. Thus, considering these properties, all the four types of the bulk solitons produced by the continuations of the solitons at $\lambda = 0$ are hardly observable.

Figure E.14(b) illustrates the maximum growth rates, $\text{Max} [\text{Im}(\delta)]$, of the bulk solitons that are continuations of the solitons found at $\gamma = 0$. The blue and red curves represent the quasi-antisymmetric and quasi-symmetric bulk solitons, respectively. Notably, there are two branches of quasi-antisymmetric bulk solitons: one resides in the middle finite bandgap, while the other is located in the semi-infinite gap. Meanwhile, it is worth mentioning that the delocalized states arising from the quasi-antisymmetric bulk solitons are also rep-

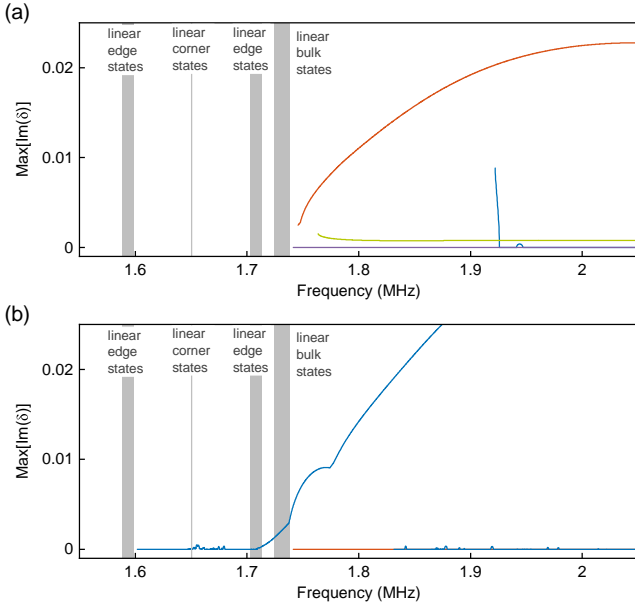
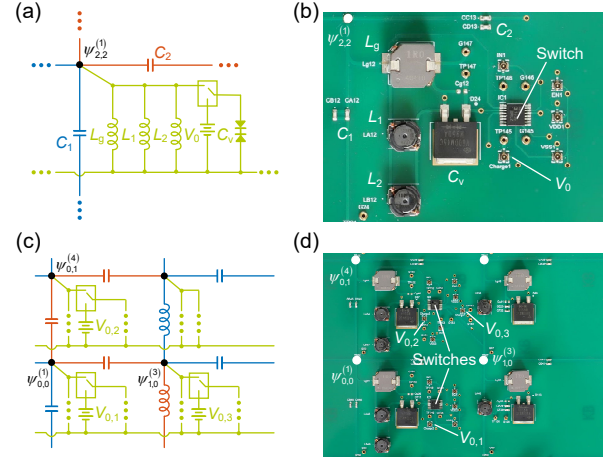


Figure E.14: **The linear stability analysis of the bulk solitons.** (a) The perturbation maximum growth rates, $\text{Max}[\text{Im}(\delta)]$, for the bulk solitons that are continuations of the solitons at $\lambda = 0$. The blue and red curves represent the quasi-antisymmetric and quasi-symmetric bulk solitons, respectively, while the yellow-green and purple curves correspond to the two types of asymmetric bulk solitons. (b) The maximum growth rates, $\text{Max}[\text{Im}(\delta)]$, of the bulk solitons that are continuations of the solitons at $\gamma = 0$. The blue and red curves denote the quasi-antisymmetric and quasi-symmetric bulk solitons, respectively. It is important to note that there are two branches of quasi-antisymmetric bulk solitons: one resides in the middle finite gap, while the other is located in the semi-infinite gap. Additionally, the delocalized states arising from the quasi-antisymmetric bulk solitons are also represented in the figure.

resented in the figure. The quasi-antisymmetric bulk solitons residing in the middle finite bandgap are generally linearly stable. Similarly, those located in the semi-infinite gap, while exhibiting weak instabilities at several frequencies, are also generally stable, particularly at frequencies near the linear bulk states. Given the strong localizations of both types of quasi-antisymmetric bulk solitons and the excellent correspondence between their state distributions and the initial three-site excitations, these solitons are expected to be experimentally observable, as supported by the experimental measurement results presented in the main text. In contrast, while the quasi-symmetric bulk solitons are linearly stable (see the red curve in Fig. E.14(b)), their localization is weak under weak nonlinearity, and their state distributions deviate from the initial excitations under strong nonlinearity (see the red curve in Fig. E.13(b)). Consequently, the quasi-symmetric bulk solitons are unlikely to be observed experimentally.

We have also conducted temporal evolutions with added noise to verify the results obtained from the linear-stability analysis. The findings are in good agreement with those presented in Fig. E.14.



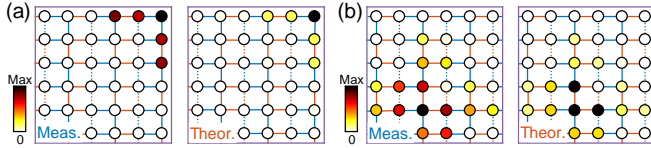


Figure F.16: **Voltage distributions in the medium-nonlinearity regime.** (a) Voltage distributions when the corner site is excited with $\psi_0 = 0.5$ V. The left side shows the measurement result, and the right side shows the theoretical prediction. (b) Voltage distributions when the three bulk sites are excited with $\psi_0 = 2.5$ V. Similarly, the left and right sides present the measurement result and the corresponding theoretical prediction, respectively.

ψ_0 , as defined in the main text. This charging operation corresponds to the preparation of the initial state. Once the SPDT switch is toggled to the circuit node, the charged diode discharges, and this discharging process represents the temporal evolution of the initial voltage distribution governed by Eqs. (B.18)–(B.21). Figure F.15(b), with important circuit components labeled in it, displays the PCB near the lattice corner. The IPEX connector labeled “Charge1” is connected to a DC voltage source, providing voltage V_0 . The IPEX connector labeled “IN1” is connected to an external digital signal generated by an arbitrary-function generator (Tektronix AFG31022), which is used to control the ON and OFF states of the SPDT switch. The voltage signals at all circuit nodes were monitored using an oscilloscope (Tektronix MDO34). This setup allows for the experimental observations of the nonlinear topological corner states and topologically trivial corner solitons.

Similarly, we implemented quench dynamics to verify the existence of the two types of bulk solitons. Unlike the single-site excitations at the lattice corner, in this case we utilized three-site excitations in the bulk of the circuit lattice. Figure F.15(c) shows a portion of the circuit diagram near the excitation sites in the bulk. For clarity’s sake, we label only the most important components in this diagram. Three SPDT switches were employed to control charging and discharging at the three lattice sites independently. Additionally, three different DC voltage sources were used, allowing the phase of the initial state to be adjusted by these voltage sources. Negative DC voltage is generated by inverting the positive voltage, using a homemade inverting amplifier. Figure F.15(d) displays the PCB near the excitation sites in the bulk. In our experiments, we utilized only two SPDT switches, as the ADG1636 switch features two independent channels. The IPEX connectors labeled “Charge2”, “Charge3”, and “Charge4” are connected to DC voltage sources providing voltages $V_{0,1}$, $V_{0,2}$, and $V_{0,3}$, respectively. These voltages satisfy the conditions $V_{0,1} = -V_{0,3} = -V_{0,2} = \psi_0$. To ensure the synchronization of the control signals between the different switches, the IPEX connectors labeled “IN2”, “IN3”, and “IN4” are connected to the same external digital signal.

After conducting the measurements, we obtained voltage distributions at different time intervals for various excitation voltages ψ_0 . The voltage envelopes were then derived from the temporal voltage signals. Taking circuit dissipation into account, we extracted the voltage distributions at $t = 9 \mu\text{s}$ for corner site excitation and at $t = 8 \mu\text{s}$ for the excitation of the

three bulk sites. The selection of these time moments ensures accurate measurement of voltage signals with negligible background noise.

For the corner site excitation, the field distributions in the weakly nonlinear regime with $\psi_0 = 0.1$ V and in the strongly nonlinear regime with $\psi_0 = 2$ V are shown in Fig. 2(d), with the corresponding theoretical predictions displayed in Fig. 2(e). The experimentally measured and theoretically predicted field distributions in the moderately nonlinear regime with $\psi_0 = 0.5$ V are presented in Fig. F.16(a). By comparing the results, we find that in the weakly nonlinear regime, the voltage distribution is localized with sublattice polarization. In the moderately nonlinear regime, although there is no apparent delocalization, we observe that the sublattice polarization is suppressed due to hybridization with the edge modes. The delocalization behavior becomes more pronounced when considering the quench dynamics over a longer time evolution (see Appendix G). In the strongly nonlinear regime, the voltage distributions exhibit strong localization, with the sublattice polarization completely disappearing.

Similarly, for the excitation at the three bulk sites, the field distributions in the weakly nonlinear regime with $\psi_0 = 0.7$ V and in the strongly nonlinear regime with $\psi_0 = 7$ V are shown in Fig. 3(c), with the corresponding theoretical predictions provided in Fig. 3(d). The experimentally measured and theoretically predicted field distributions in the moderately nonlinear regime with $\psi_0 = 2.5$ V are illustrated in Fig. F.16(b). By comparing the results, we find that in both the weakly and strongly nonlinear regimes, the voltage distributions are localized. In contrast, in the moderately nonlinear regime, there is apparent delocalization. Thus, as nonlinearity increases, we observe a transition from localization to delocalization and back to localization. Furthermore, this transition becomes more pronounced when considering the quench dynamics over longer time evolution (see Appendix G).

Appendix G. The quench dynamics in longer time evolution

Due to the inherent circuit dissipation that limits experimental quench dynamics, we have theoretically investigated the quench dynamics in the course of longer evolution. Unlike the relatively short evolution observed in Figs. 2 and 3 of the main text, which are limited to $t = 9 \mu\text{s}$ and $t = 8 \mu\text{s}$, respectively, we have here examined the evolution extending up to $50 \mu\text{s}$.

First, we investigated the case of excitations at a single corner site, confirming the existence of persistent nonlinear topological corner states and topologically trivial corner solitons. As shown in Fig. G.17(a), the IPRs of the voltage distributions for different initial voltages ψ_0 again exhibit the localization-delocalization-localization transition, which is analyzed in detail in the main text. The corresponding voltage distributions are localized for both small and large initial voltages, while they are evidently delocalized for medium initial voltages, as illustrated by the distributions at three representative values of ψ_0 shown in the insets. The results produced by the prolonged evolution are consistent with those presented in the main text. This

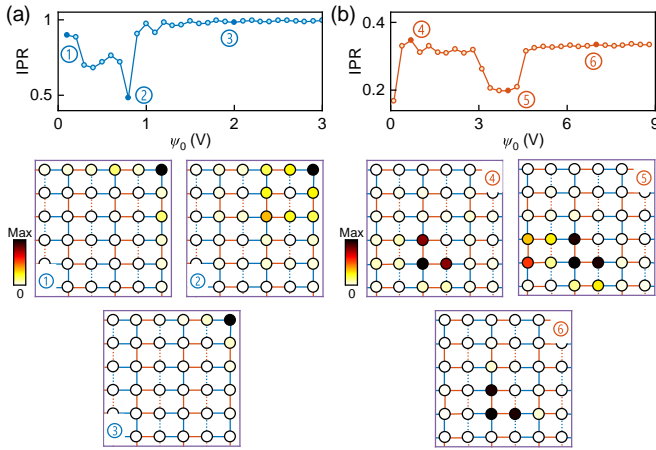


Figure G.17: **The quench dynamics, as displayed by the longer evolution.** (a)-(b) IPRs of the voltage distributions for different initial voltages, with insets displaying the voltage distributions at representative values of ψ_0 . Panels (a) and (b) correspond to the excitation applied at a single corner site and three bulk sites, respectively.

indicates that, for small initial voltages, the nonlinear corner states are excited as long-lived ones by the quench dynamics. Similarly, long-lived corner solitons are efficiently excited for large initial voltages. At medium values of ψ_0 , the voltage distributions become relatively delocalized, as there are no localized states persisting in the medium-nonlinearity regime. For small initial voltages, there is a slight difference between the results of the extended and short-time evolution. This discrepancy arises from the differences between the input distributions and the eigenstates of the nonlinear corner states.

Second, we investigated the excitation at three bulk lattice sites, reconfirming the existence of two types of the bulk solitons. As shown in Fig. G.17(b), the IPRs of the voltage distributions for different initial voltages ψ_0 definitely exhibit the localization-delocalization-localization transition. The voltage distributions are localized for both small and large initial voltages, while they are evidently delocalized for medium initial voltages, as illustrated by the distributions at three representative values of ψ_0 shown in the insets. For the first initial voltage, $\psi_0 = 0.1$ V, the IPR is small because the bulk soliton demonstrates very weak localization in the case of weak nonlinearity (see also Appendix E). The results produced by the extended evolution are again consistent with those presented in the main text, indicating that, for small initial voltages, the bulk solitons residing in the middle finite gap are definitely excited by the quench dynamics. Similarly, the bulk solitons located in the semi-infinite gap can also be effectively excited for large initial voltages. At medium values of ψ_0 , the voltage distributions become relatively delocalized, as there are no localized states maintained by medium-strength nonlinearities. For small initial voltages, a discrepancy exists between the results of the extended and short-time evolution. It arises because the voltage distribution in the bulk solitons residing in the middle finite bandgap cannot be accurately captured by the input distribution, such as those with $\psi_{0,0}^{(1)} = \psi_0$ and $\psi_{1,0}^{(3)} = \psi_{0,1}^{(4)} = -\psi_0$.

Appendix H. The summary of the work

Based on the previous discussions, here we would like to summarize the concept of the NLQTIs adopted in the present work and our main findings.

Building on the seminal lattice model for a linear QTI [3], we have introduced onsite nonlinearity. In contrast to the QTI with externally controlled hoppings [75], our system is intrinsically nonlinear due to the self-interactions. As shown in Fig. H.18(a), when the corner site of the NLQTI is excited at low intensity, the field distribution remains localized at the corner, forming nonlinear topological corner states in the weakly nonlinear regime. As the excitation intensity increases, the field distribution spreads out, as the nonlinear corner states become delocalized in the regime of the moderately nonlinearity strength (due to the fact that the respective solution branch passes through a band of linear edge states). At high excitation intensities, the field localizes again in the form of topologically trivial corner solitons in the strongly nonlinear regime. A localization-delocalization-localization transition, similar to what we find in the NLQTIs, was observed in a nonlinear Wannier-type HOTI [74]. Furthermore, we investigate the field distributions when inner sites of the lattice (rather than the corner one) are locally excited with varying intensities, as shown in Fig. H.18(b). In this case, the field distribution again exhibits a localized-delocalized-localized transition. The initial localized distribution corresponds to a bulk soliton hosted by the middle finite gap in the weakly nonlinear regime, while the final localized distribution corresponds to a bulk soliton hosted by the semi-infinite gap in the case of strong nonlinearity.

Appendix I. Comparison with nonlinear Wannier-type higher-order topological insulators

In this section, we compare our NLQTI with the previous experimental realizations of nonlinear Wannier-type HOTIs. In 2019, Zangeneh-Nejad et al. proposed the concept of nonlinear second-order TIs and demonstrated that zero-dimensional corner states can be induced in a trivial insulator by increasing the external pump intensity [72]. The key to their implementation lies in the nonlinear coupling coefficients of the Wannier-type HOTI. Under weak nonlinearity, their structure is a trivial insulator, lacking localized states in both the bulk and corner regions. Under strong nonlinearity, their structure transitions to a Wannier-type HOTI that supports localized corner states. In comparison, our NLQTI enables nonlinearity-controlled switching between two types of localized states. Under weak nonlinearity, our NLQTI supports nonlinear topological corner states and bulk solitons residing in the middle finite gap. Under strong nonlinearity, it supports topologically trivial corner solitons and bulk solitons residing in the semi-infinite gap. This localization-delocalization-localization transition enhances the active manipulation of field distributions in HOTIs and may have applications in photonics and cold atomic systems.

In 2021, Hu et al. [73] and Kirsch et al. [74] independently realized nonlinear second-order photonic TIs. Both their

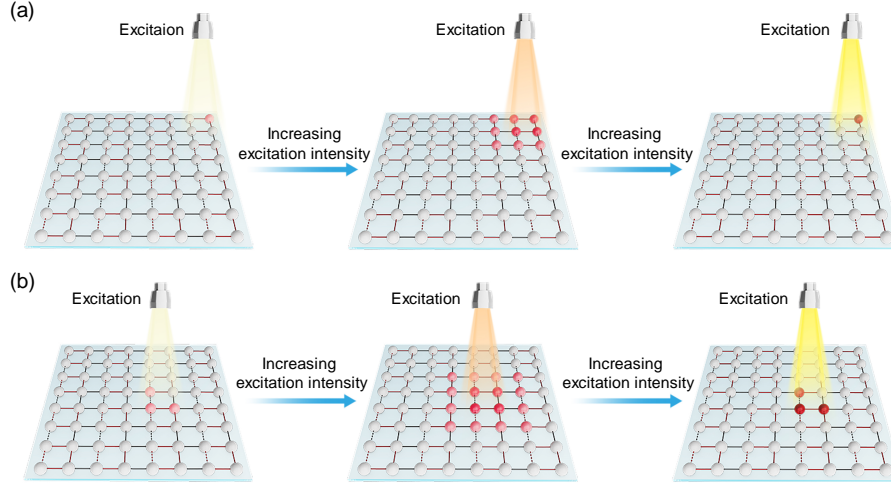


Figure H.18: **NLQTIs in the system with the onsite nonlinearity are displayed by means of the field distributions corresponding to varying excitation intensities.** (a) At a low intensity, the field distribution is localized around the corner site, in form of nonlinear topological corner states. As the excitation intensity increases, the field spreads out, making the nonlinear corner states delocalized. At high intensities, the field again gets tightly localized close to the corner site, forming topologically trivial corner solitons. (b) When inner sites (rather than the corner) are excited with different intensities, the field distribution undergoes a localization-delocalization-localization transition as well. The initial localized distribution corresponds to a bulk soliton belonging to the middle finite gap in the case of weak nonlinearity, while the final localized distribution corresponds to a bulk soliton residing in the the semi-infinite gap, in the strong-nonlinearity regime.

second-order TIs belong to the Wannier type, with nonlinearity introduced through the onsite energies. Hu et al. utilized a 2D Su-Schrieffer-Heeger (SSH) lattice that supports higher-order topological bound states in the continuum (BICs) [73]. In this configuration, the corner-localized states are embedded within the continuum of the bulk bands rather than in the band gap [85, 86]. Under weak nonlinearity, Hu et al. do not observe stationary beam dynamics; instead, they find that the corner mode undergoes beating with the edge modes. In contrast, our NLQTI supports stationary dynamics in both weakly and strongly nonlinear regimes. The corner states of our QTI are stably separated from other states, avoiding coupling between the corner states and edge states, as long as the frequency is kept below the band of the linear edge states.

Kirsch et al. experimentally explored the nonlinear dynamics of light in photonic HOTIs based on a kagome lattice [74]. Through the observation of stationary beam dynamics, they identified the formation of nonlinear topological corner states, as well as topologically trivial corner solitons. A notable limitation of the kagome lattice is that the corner states reside within the continuum of bulk modes when the lattice dimerizations are weak, even though the topological invariants remain non-vanishing. This limitation restricts the range of existence for localized nonlinear corner states and imposes strict requirements on the lattice parameters. In contrast, the corner states of our QTI are stably separated from other states, even in weakly dimerized lattices, as long as the quadrupole moment remains nonzero. This feature enables the realization of well-localized nonlinear corner states and bulk solitons across a broader range of frequencies, alleviating the stringent requirements on lattice parameters.

References

- [1] M. Z. Hasan and C. L. Kane, Colloquium: Topological insulators, *Rev. Mod. Phys.* 82, 3045 (2010).
- [2] X.-L. Qi and S.-C. Zhang, Topological insulators and superconductors, *Rev. Mod. Phys.* 83, 1057 (2011).
- [3] W. A. Benalcazar, B. A. Bernevig, and T. L. Hughes, Quantized electric multipole insulators, *Science* 357, 61 (2017).
- [4] W. A. Benalcazar, B. A. Bernevig, and T. L. Hughes, Electric multipole moments, topological multipole moment pumping, and chiral hinge states in crystalline insulators, *Phys. Rev. B* 96, 245115 (2017).
- [5] M. Serra-Garcia, V. Peri, R. Süssstrunk, O. R. Bilal, T. Larsen, L. G. Villanueva, and S. D. Huber, Observation of a phononic quadrupole topological insulator, *Nature* 555, 342 (2018).
- [6] C. W. Peterson, W. A. Benalcazar, T. L. Hughes, and G. Bahl, A quantized microwave quadrupole insulator with topologically protected corner states, *Nature* 555, 346 (2018).
- [7] S. Mittal, V. V. Orre, G. Zhu, M. A. Gorlach, A. Poddubny, and M. Hafezi, Photonic quadrupole topological phases, *Nature Photon.* 13, 692 (2019).
- [8] S. Imhof, C. Berger, F. Bayer, J. Brehm, L. W. Molenkamp, T. Kiessling, F. Schindler, C. H. Lee, M. Greiter, T. Neupert, and R. Thomale, Topolectrical-circuit realization of topological corner modes, *Nature Phys.* 14, 925 (2018).

[9] S. Liu, S. Ma, Q. Zhang, L. Zhang, C. Yang, O. You, W. Gao, Y. Xiang, T. J. Cui, and S. Zhang, Octupole corner state in a three-dimensional topological circuit, *Light: Science & Applications* 9, 1 (2020).

[10] J. Bao, D. Zou, W. Zhang, W. He, H. Sun, and X. Zhang, Topoelectrical circuit octupole insulator with topologically protected corner states, *Phys. Rev. B* 100, 201406 (2019).

[11] W. Zhang, D. Zou, J. Bao, W. He, Q. Pei, H. Sun, and X. Zhang, Topoelectrical-circuit realization of a four-dimensional hexadecapole insulator, *Phys. Rev. B* 102, 100102 (2020).

[12] X. Ni, M. Li, M. Weiner, A. Alù, and A. B. Khanikaev, Demonstration of a quantized acoustic octupole topological insulator, *Nat. Commun.* 11, 2108 (2020).

[13] Y. Qi, C. Qiu, M. Xiao, H. He, M. Ke, and Z. Liu, Acoustic Realization of Quadrupole Topological Insulators, *Phys. Rev. Lett.* 124, 206601 (2020).

[14] H. Xue, Y. Ge, H.-X. Sun, Q. Wang, D. Jia, Y.-J. Guan, S.-Q. Yuan, Y. Chong, and B. Zhang, Observation of an acoustic octupole topological insulator, *Nat. Commun.* 11, 2442 (2020).

[15] X. Zhang, Z.-K. Lin, H.-X. Wang, Z. Xiong, Y. Tian, M.-H. Lu, Y.-F. Chen, and J.-H. Jiang, Symmetry-protected hierarchy of anomalous multipole topological band gaps in nonsymmorphic metacrystals, *Nat. Commun.* 11, 65 (2020).

[16] D. Cai, A. R. Bishop, and N. Grønbech-Jensen, Localized states in discrete nonlinear Schrödinger equation, *Phys. Rev. Lett.* 72, 591–595 (1994).

[17] Y. Lahini, A. Avidan, F. Pozzi, M. Sorel, R. Morandotti, D. N. Christodoulides, and I. Silberberg, Anderson localization and nonlinearity in one-dimensional disordered photonic lattices, *Phys. Rev. Lett.* 100, 013906 (2008).

[18] M. Ezawa, Higher-Order Topological Insulators and Semimetals on the Breathing Kagome and Pyrochlore Lattices, *Phys. Rev. Lett.* 120, 026801 (2018).

[19] M. Ezawa, Minimal models for Wannier-type higher-order topological insulators and phosphorene, *Phys. Rev. B* 98, 045125 (2018).

[20] X. Ni, M. Weiner, A. Alù, and A. B. Khanikaev, Observation of higher-order topological acoustic states protected by generalized chiral symmetry, *Nature Mater.* 18, 113 (2019).

[21] H. Xue, Y. Yang, F. Gao, Y. Chong, and B. Zhang, Acoustic higher-order topological insulator on a kagome lattice, *Nature Mater.* 18, 108 (2019).

[22] J. Noh, W. A. Benalcazar, S. Huang, M. J. Collins, K. P. Chen, T. L. Hughes, and M. C. Rechtsman, Topological protection of photonic mid-gap defect modes, *Nature Photon.* 12, 408 (2018).

[23] X. Zhang, H.-X. Wang, Z.-K. Lin, Y. Tian, B. Xie, M.-H. Lu, Y.-F. Chen, and J.-H. Jiang, Second-order topology and multidimensional topological transitions in sonic crystals, *Nat. Phys.* 15, 582 (2019).

[24] B.-Y. Xie, G.-X. Su, H.-F. Wang, H. Su, X.-P. Shen, P. Zhan, M.-H. Lu, Z.-L. Wang, and Y.-F. Chen, Visualization of Higher-Order Topological Insulating Phases in Two-Dimensional Dielectric Photonic Crystals, *Phys. Rev. Lett.* 122, 233903 (2019).

[25] S. N. Kempkes, M. R. Slot, J. J. van den Broeke, P. Capiod, W. A. Benalcazar, D. Vanmaekelbergh, D. Bercioux, I. Swart, and C. Morais Smith, Robust zero-energy modes in an electronic higher-order topological insulator, *Nat. Mater.* 18, 1292 (2019).

[26] H. Fan, B. Xia, L. Tong, S. Zheng, and D. Yu, Elastic Higher-Order Topological Insulator with Topologically Protected Corner States, *Phys. Rev. Lett.* 122, 204301 (2019).

[27] X.-D. Chen, W.-M. Deng, F.-L. Shi, F.-L. Zhao, M. Chen, and J.-W. Dong, Direct Observation of Corner States in Second-Order Topological Photonic Crystal Slabs, *Phys. Rev. Lett.* 122, 233902 (2019).

[28] A. El Hassan, F. K. Kunst, A. Moritz, G. Andler, E. J. Bergholtz, and M. Bourennane, Corner states of light in photonic waveguides, *Nature Photon.* 13, 697 (2019).

[29] M. Weiner, X. Ni, M. Li, A. Alù, and A. B. Khanikaev, Demonstration of a third-order hierarchy of topological states in a three-dimensional acoustic metamaterial, *Sci. Adv.* 6, eaay4166 (2020).

[30] X. Zhang, B.-Y. Xie, H.-F. Wang, X. Xu, Y. Tian, J.-H. Jiang, M.-H. Lu, and Y.-F. Chen, Dimensional hierarchy of higher-order topology in three-dimensional sonic crystals, *Nat. Commun.* 10, 5331 (2019).

[31] Z. Wang, Y. Meng, B. Yan, D. Zhao, L. Yang, J. Chen, M. Cheng, T. Xiao, P. P. Shum, G.-G. Liu, Y. Yang, H. Chen, X. Xi, Z. Zhu, B. Xie, and Z. Gao, Realization of a three-dimensional photonic higher-order topological insulator, *Nat. Commun.* 16, 3122 (2025).

[32] D. Smirnova, D. Leykam, Y. Chong, and Y. Kivshar, Nonlinear topological photonics, *Appl. Phys. Rev.* 7, 021306 (2020).

[33] A. Szameit and M. C. Rechtsman, Discrete nonlinear topological photonics, *Nature Phys.* 20, 905 (2024).

[34] H. Sahin, H. Akgün, Z. B. Siu, S. M. Rafi-Ul-Islam, J. F. Kong, M. B. A. Jalil, and C. H. Lee, Protected Chaos in a Topological Lattice, *Adv. Sci.* 12, e03216 (2025).

[35] H. Sahin, M. B. A. Jalil, and C. H. Lee, Topoelectrical Circuits – Recent Experimental Advances and Developments, *APL Electronic Devices* 1, 021503 (2025).

[36] H. Yang, L. Song, Y. Cao, and P. Yan, Circuit realization of topological physics, *Phys. Rep.* 1093, 1 (2024).

[37] H. Zhong, V. O. Kompanets, Y. Zhang, Y. V. Kartashov, M. Cao, Y. Li, S. A. Zhuravitskii, N. N. Skryabin, I. V. Dyakonov, A. A. Kalinkin, S. P. Kulik, S. V. Chekalin, and V. N. Zadkov, Observation of nonlinear fractal higher order topological insulator, *Light Sci. Appl.* 13, 264 (2024).

[38] B. A. Malomed, Prediction and observation of topological modes in fractal nonlinear optics, *Light Sci. Appl.* 14, 29 (2025).

[39] V. O. Kompanets, S. Feng, Y. Zhang, Y. V. Kartashov, Y. Li, S. A. Zhuravitskii, N. N. Skryabin, A. V. Kireev, I. V. Dyakonov, A. A. Kalinkin, C. Shang, S. P. Kulik, S. V. Chekalin, and V. N. Zadkov, Observation of Nonlinear Topological Corner States Originating from Different Spectral Charges, *Adv. Mater.* 37, 2500556 (2025).

[40] C. Huang, A. V. Kireev, Y. Jiang, V. O. Kompanets, C. Shang, Y. V. Kartashov, S. A. Zhuravitskii, N. N. Skryabin, I. V. Dyakonov, A. A. Kalinkin, S. P. Kulik, F. Ye, and V. N. Zadkov, Observation of nonlinear higher-order topological insulators with unconventional boundary truncations, *Commun. Phys.* 8, 451 (2025).

[41] M. J. Ablowitz, C. W. Curtis, and Y.-P. Ma, Linear and nonlinear traveling edge waves in optical honeycomb lattices, *Phys. Rev. A* 90, 023813 (2014).

[42] D. Leykam and Y. D. Chong, Edge Solitons in Nonlinear-Photonic Topological Insulators, *Phys. Rev. Lett.* 117, 143901 (2016).

[43] Y. Lumer, M. C. Rechtsman, Y. Plotnik, and M. Segev, Instability of bosonic topological edge states in the presence of interactions, *Phys. Rev. A* 94, 021801 (2016).

[44] Y. V. Kartashov, A. A. Arkhipova, S. A. Zhuravitskii, N. N. Skryabin, I. V. Dyakonov, A. A. Kalinkin, S. P. Kulik, V. O. Kompanets, S. V. Chekalin, L. Torner, and V. N. Zadkov, Observation of Edge Solitons in Topological Trimer Arrays, *Phys. Rev. Lett.* 128, 093901 (2022).

[45] S. D. Hashemi and S. Mittal, Floquet topological dissipative Kerr solitons and incommensurate frequency combs, *Nat. Commun.* 15, 9642 (2024).

[46] S. Mukherjee and M. C. Rechtsman, Observation of Unidirectional Solitonlike Edge States in Nonlinear Floquet Topological Insulators, *Phys. Rev. X* 11, 041057 (2021).

[47] D. A. Dobrykh, A. V. Yulin, A. P. Slobozhanyuk, A. N. Poddubny, and Yu. S. Kivshar, Nonlinear Control of Electromagnetic Topological Edge States, *Phys. Rev. Lett.* 121, 163901 (2018).

[48] Z. Hu, D. Bongiovanni, D. Jukić, E. Jajtić, S. Xia, D. Song, J. Xu, R. Morandotti, H. Buljan, and Z. Chen, Nontrivial coupling of light into a defect: the interplay of nonlinearity and topology, *Light Sci. Appl.* 9, 147 (2020).

[49] T. Tuloup, R. W. Bomantara, C. H. Lee, and J. Gong, Nonlinearity induced topological physics in momentum space and real space, *Phys. Rev. B* 102, 115411 (2020).

[50] K. Bai, J.-Z. Li, T.-R. Liu, L. Fang, D. Wan, and M. Xiao, Arbitrarily Configurable Nonlinear Topological Modes, *Phys. Rev. Lett.* 133, 116602 (2024).

[51] K. Sone, M. Ezawa, Z. Gong, T. Sawada, N. Yoshioka, and T. Sagawa, Transition from the topological to the chaotic in the nonlinear Su-Schrieffer-Heeger model, *Nat. Commun.* 16, 422 (2025).

[52] Z. Zhang, R. Wang, Y. Zhang, Y. V. Kartashov, F. Li, H. Zhong, H. Guan, K. Gao, F. Li, Y. Zhang, and M. Xiao, Observation of edge solitons in photonic graphene, *Nat. Commun.* 11, 1902 (2020).

[53] S. Mittal, G. Moille, K. Srinivasan, Y. K. Chembo, and M. Hafezi, Topological frequency combs and nested temporal solitons, *Nat. Phys.* 17, 1169 (2021).

[54] C. J. Flower, M. Jalali Mehrabad, L. Xu, G. Moille, D. G. Suarez-Forero, O. Örsel, G. Bahl, Y. Chembo, K. Srinivasan, S. Mittal, M. Hafezi, Observation of topological frequency combs, *Science* 384, 1356 (2024).

[55] R. Li, W. Wang, X. Kong, C. Shang, Y. Jia, G.-G. Liu, Y. Liu, and B. Zhang, Self-Induced Topological Edge States in a Lattice with Onsite Nonlinearity, *arXiv:2504.11964* (2025).

[56] Y. Lumer, Y. Plotnik, M. C. Rechtsman, and M. Segev, Self-Localized States in Photonic Topological Insulators, *Phys. Rev. Lett.* 111, 243905 (2013).

[57] S. Mukherjee and M. C. Rechtsman, Observation of Floquet solitons in a topological bandgap, *Science* 368, 856 (2020).

[58] S. Mukherjee and M. C. Rechtsman, Period-doubled Floquet solitons, *Optica* 10, 1310 (2023).

[59] G. Liu, J. Noh, J. Zhao, and G. Bahl, Self-Induced Dirac Boundary State and Digitization in a Nonlinear Resonator Chain, *Phys. Rev. Lett.* 129, 135501 (2022).

[60] N. Pernet, P. St-Jean, D. D. Solnyshkov, G. Malpuech, N. C. Zambon, Q. Fontaine, B. Real, O. Jamadi, A. Lemaître, M. Morassi, L. L. Gratiet, T. Baptiste, A. Harouri, I. Sagnes, A. Amo, S. Ravets, and J. Bloch, Gap solitons in a one-dimensional driven-dissipative topological lattice, *Nat. Phys.* 18, 678 (2022).

[61] D. D. Solnyshkov, O. Bleu, B. Teklu, and G. Malpuech, Chirality of Topological Gap Solitons in Bosonic Dimer Chains, *Phys. Rev. Lett.* 118, 023901 (2017).

[62] D. A. Smirnova, L. A. Smirnov, D. Leykam, and Y. S. Kivshar, Topological Edge States and Gap Solitons in the Nonlinear Dirac Model, *Laser & Photonics Reviews* 13, 1900223 (2019).

[63] R. Li, X. Kong, D. Hang, G. Li, H. Hu, H. Zhou, Y. Jia, P. Li, and Y. Liu, Topological bulk solitons in a nonlinear photonic Chern insulator, *Commun. Phys.* 5, 275 (2022).

[64] R. Li, P. Li, Y. Jia, and Y. Liu, Self-localized topological states in three dimensions, *Phys. Rev. B* 105, L201111 (2022).

[65] Y.-L. Tao, N. Dai, Y.-B. Yang, Q.-B. Zeng, and Y. Xu, Hinge solitons in three-dimensional second-order topological insulators, *New J. Phys.* 22, 103058 (2020).

[66] Y. Zhang, Y. V. Kartashov, L. Torner, Y. Li, and A. Ferrando, Nonlinear higher-order polariton topological insulator, *Opt. Lett.* 45, 4710 (2020).

[67] M. Ezawa, Nonlinearity-induced transition in the nonlinear Su-Schrieffer-Heeger model and a nonlinear higher-order topological system, *Phys. Rev. B* 104, 235420 (2021).

[68] S. K. Ivanov, Y. V. Kartashov, and L. Torner, Light bullets in Su-Schrieffer-Heeger photonic topological insulators, *Phys. Rev. A* 107, 033514 (2023).

[69] Y. V. Kartashov, Solitons in higher-order topological insulator created by unit cell twisting, *Chaos, Solitons & Fractals* 185, 115188 (2024).

[70] K. Prabith, G. Theocharis, and R. Chaunsali, Nonlinear corner states in a topologically nontrivial kagome lattice, *Phys. Rev. B* 110, 104307 (2024).

[71] J. Yi and C. Q. Chen, Delocalization and higher-order topology in a nonlinear elastic lattice, *New J. Phys.* 26, 063004 (2024).

[72] F. Zangeneh-Nejad and R. Fleury, Nonlinear Second-Order Topological Insulators, *Phys. Rev. Lett.* 123, 053902 (2019).

[73] Z. Hu, D. Bongiovanni, D. Jukić, E. Jajtić, S. Xia, D. Song, J. Xu, R. Morandotti, H. Buljan, and Z. Chen, Nonlinear control of photonic higher-order topological bound states in the continuum, *Light Sci. Appl.* 10, 164 (2021).

[74] M. S. Kirsch, Y. Zhang, M. Kremer, L. J. Maczewsky, S. K. Ivanov, Y. V. Kartashov, L. Torner, D. Bauer, A. Szaimeit, and M. Heinrich, Nonlinear second-order photonic topological insulators, *Nat. Phys.* 17, 995 (2021).

[75] M. Serra-Garcia, R. Süsstrunk, and S. D. Huber, Observation of quadrupole transitions and edge mode topology in an LC circuit network, *Phys. Rev. B* 99, 020304 (2019).

[76] Y. V. Kartashov, B. A. Malomed, and L. Torner, Solitons in nonlinear lattices, *Rev. Mod. Phys.* 83, 247 (2011).

[77] F. Lederer, G. I. Stegeman, D. N. Christodoulides, G. Assanto, M. Segev, and Y. Silberberg, Discrete solitons in optics, *Phys. Rep.* 463, 1 (2008).

[78] Z. Chen, M. Segev, and D. N. Christodoulides, Optical spatial solitons: historical overview and recent advances, *Rep. Prog. Phys.* 75, 086401 (2012).

[79] L. Wang, Z. Yan, Y. Zhu, and J. Zeng, Gap solitons and vortices in two-dimensional spin-orbit-coupled Bose-Einstein condensates loaded onto moiré optical lattices, *Quantum. Front.* 4, 9 (2025).

[80] R. Liquito, M. Gonçalves, and E. Castro, Quasiperiodic quadrupole insulators, *SciPost Phys.* 18, 208 (2025).

[81] R. Li, X. Kong, W. Wang, Y. Wang, Y. Jia, H. Tao, P. Li, Y. Liu, and B. A. Malomed, Observation of edge solitons and transitions between them in a trimer circuit lattice, *Commun. Phys.* 8, 342 (2025).

[82] S. Aubry, breathers in nonlinear lattices: Existence, linear stability and quantization, *Physica D* 103, 201 (1997).

[83] H. A. Gersch and G. C. Knollman, Quantum Cell Model for Bosons, *Phys. Rev.* 129, 959 (1963).

[84] Y. Hadad, J. C. Soric, A. B. Khanikaev, and A. Alù, Self-Induced Topological Protection in Nonlinear Circuit Arrays, *Nat. Electron.* 1, 178 (2018).

[85] W. A. Benalcazar and A. Cerjan, Bound states in the continuum of higher-order topological insulators, *Phys. Rev. B* 101, 161116 (2020).

[86] A. Cerjan, M. Jürgensen, W. A. Benalcazar, S. Mukherjee, and M. C. Rechtsman, Observation of a Higher-Order Topological Bound State in the Continuum, *Phys. Rev. Lett.* 125, 213901 (2020).